Nanostructured system based on hydroxyapatite and curcumin: A promising candidate for osteosarcoma therapy

Pauline Nunes Marinho, Jéssica ; Paz Neme, Natália; Josue de Souza Matos, Matheus; Junio Campos Batista, Ronaldo ; Augusto de Almeida Macedo, Waldemar; Lana Gastelois, Pedro ; Assis GomesDawidson Assis Gomes, Dawidson; Angela RodriguesAngela RodriguesAngela RodriguesAngela Rodrigues, Michele ; Fernandes CipresteMarcelo Fernandes CipresteMarcelo Fernandes Cipreste, Marcelo ; Martins Barros Sousa, Edésia

Published in:
Ceramics International

DOI:
10.1016/j.ceramint.2023.03.115

Document Version
Publisher's PDF, also known as Version of record

Publication date:
2023

Ceramics International 49 (2023) 19932–19949

Contents lists available at ScienceDirect

Ceramics International

journal homepage: www.elsevier.com/locate/ceramint

Nanostructured system based on hydroxyapatite and curcumin: A promising candidate for osteosarcoma therapy

Jéssica Pauline Nunes Marinho [a], Natalia Paz Neme [b], Matheus Josue de Souza Matos [c], Ronaldo Junio Campos Batista [c], Waldemar Augusto de Almeida Macedo [a], Pedro Lana Gastelois [a], Dawidson Assis Gomes [d], Michele Angela Rodrigues [a], Marcelo Fernandes Cipreste [a,1], Edésia Martins Barros de Sousa [a,*]

[a] Centro de Desenvolvimento da Tecnologia Nuclear – CDTN, Avenida Presidente Antônio Carlos, 6.627 - Campus UFMG, CEP, 31270-901, Belo Horizonte, Minas Gerais, Brazil
[b] Zernike Institute for Advanced Materials and Stratingh Institute for Chemistry, University of Groningen, Nijenborgh 4, 9747, AG Groningen, the Netherlands
[c] Departamento de Física, Universidade Federal de Ouro Preto - UFOP, Rua Diogo de Vasconcelos, CEP 12235400-000, Ouro Preto, MG, Brazil
[d] Departamento de Bioquímica e Imunologia, Instituto de Ciências Biológicas, Universidade Federal de Minas Gerais - UFMG, Avenida Presidente Antônio Carlos, 6.627, CEP, 31270-901, Belo Horizonte, Minas Gerais, Brazil

ARTICLE INFO

Handling Editor: P. Vincenzini

Keywords:
Nanostructures
Curcumin
Hydroxyapatite
Osteosarcoma

ABSTRACT

Osteosarcoma is the most common type of bone cancer. Despite therapeutic progress, survival rates for metastatic cases or that do not respond well to chemotherapy remain in the 30% range. In this sense, the use of nanotechnology to develop targeted and more effective therapies is a promising tool in the fight against cancer. Nanostructured hydroxyapatite, due to its biocompatibility and the wide possibility of functionalization, is an interesting material to design nanoplatforms for targeted drug delivery. These platforms have the potential to enable the use of natural substances in the fight against cancer, such as curcumin. Curcumin is a polyphenol with promising properties in treating various types of cancer, including osteosarcoma. In this work, hydroxyapatite (n-HA) nanorods synthesized by the hydrothermal method were investigated as a carrier for curcumin. For this, first-principle calculations based on the Density Functional Theory (DFT) were performed, in which the modification of curcumin (CM) with the coupling agent (3-aminopropyl) triethoxysilane (APTES) was theoretically evaluated. Curcumin was incorporated in n-HA and the drug loading stability was evaluated by leaching test. Samples were characterized by a multi-techniques approach, including Fourier transform infrared spectroscopy (FTIR), UV–visible spectroscopy (UV–Vis), X-ray diffraction (XRD), X-ray fluorescence spectrometry (FRX), thermogravimetric analysis (TGA), differential scanning calorimetry (DSC), zeta potential analysis (ζ), X-ray photoelectron spectroscopy (XPS) and transmission electron microscopy (TEM). The results show that n-HAs with a 90 nm average size were obtained and successful incorporation of curcumin in the nanostructure was achieved. Cell viability and the number of osteosarcoma cells were decreased by CMAP-HA treatment. Furthermore, the stability test suggests that hydroxyapatite nanoparticles present great potential for the transportation of curcumin in the bloodstream, crediting this system for biological performance evaluations aiming at the treatment of osteosarcomas. Keywords: nanostructures, curcumin, hydroxyapatite, osteosarcoma.

1. introduction

Osteosarcoma is the most common type of primary bone neoplasm that mainly affects metaphyseal regions of long bones in which malignant cells produce immature bone tissue. Although it can occur at any age, the incidence of this cancer is more frequent in children and adolescents [1–3]. Osteosarcoma is considered a rare type of cancer; its global incidence is 1–3 cases per million people annually on average [4–8]. The high mortality rate is associated with easily spreading of metastatic cells to distant sites [9]. Most osteosarcomas are highly

* Corresponding author.
E-mail address: sousaem@cdtn.br (E.M.B. Sousa).
[1] Current address: JHS Biomateriais. Rua Ouro Branco, 345 – Sabará/MG.

https://doi.org/10.1016/j.ceramint.2023.03.115
Received 24 November 2022; Received in revised form 27 February 2023; Accepted 11 March 2023
Available online 16 March 2023

aggressive, about 20% of patients already have some type of detectable metastasis on imaging diagnosis, while approximately 90% of patients already have some metastatic lesion, mainly in the lungs, which are not yet detectable at the time of diagnosis [10].

Currently, the standard treatment used in osteosarcoma is based on the combination of surgery and systemic, neoadjuvant, and adjuvant multimodal chemotherapy [1–3]. Usually, treatments with chemotherapy apply high doses of two or more drugs together, which generates several side effects and can cause damage to healthy tissues and other organs [11]. The surgical process aims at the total resection of the tumor, including a part of the surrounding healthy tissue. However, it is not always possible to perform limb-sparing surgery and in some cases, amputation may be the best option to prevent recurrence [1–3]. Radiotherapy is not a widely used strategy in the treatment of osteosarcoma, due to its low sensitivity to ionizing radiation [12]. It may be recommended in cases where complete surgical removal of the primary tumor is not possible or when it is not possible to obtain clean margins in surgery [5,11]. Before the mid-1970s, amputation was the treatment performed in most cases of osteosarcoma, and the 5-year relative survival rate after diagnosis of the disease was approximately 20% [6,8]. With the introduction of neoadjuvant chemotherapy, there was an increase in the survival rate to about 70% in cases of localized osteosarcoma. However, for recurrent metastatic and chemoresistant cases, the survival rate remains in the range of 20% [13,14]. Despite the advances achieved with neoadjuvant chemotherapy and the various attempts with different chemotherapy regimens in recent decades, there has not been a significant improvement in the survival rate for those osteosarcoma cases that did not respond well to treatments [6,12,15]. Due to such difficulties, there is a real need for new treatment options that are more effective, capable of inhibiting the progression of the disease and the appearance of metastases, minimizing side effects, and improving the quality of life of patients.

Over the years, several natural products have been used in the treatment of diseases or the development of new drugs [16]. Curcumin (CM), the main bioactive component of Turmeric Longa L, also known as turmeric, has been used for over 2000 years in the treatment of diseases [17,18]. Research and clinical trials carried out in recent decades have confirmed its anti-inflammatory, antioxidant, and anti-carcinogenic properties, as well as its potential therapeutic effect in the treatment of various types of cancer, including osteosarcoma [19].

The unique properties of CM enhance its ability to act on various signaling pathways, in addition to its ability to effectively eliminate reactive oxygen and nitrogen species and inhibit lipid peroxidation [20]. Studies regarding the biomedical mechanism of curcumin indicate that it exhibits an effect on the pathogenesis of osteosarcoma through different pathways. At the molecular level, curcumin not only inhibits cell proliferation and metastasis, but also induces apoptosis through the modulation of various pro-inflammatory factors, including for example growth factor receptors, inflammatory cytokines, transcription factors, enzymes, kinases, and adhesion molecules, among others [21]. CM has the ability to directly inhibit a wide group of proteins responsible for cell growth, proliferation, cell cycle control, migration, and inhibition of apoptosis [22]. In addition, it modulates many signaling pathways that are dependent on tyrosine kinases. This pleiotropic characteristic of CM is in line with current trends in oncology pharmacology, offering a lower risk of resistance, which is often observed in the use of standard tyrosine kinase inhibitors [22]. An in vivo study examined the cytotoxic effect of curcumin on seven osteosarcoma cell lines with varying degrees of metastatic potential. Curcumin inhibited the growth of all osteosarcoma cell lines in addition to inhibiting their migration [23]. Wang et al. [24] demonstrated that free curcumin and its encapsulated form in a mixed system of biopolymers were able to inhibit the proliferation, migration, and invasion of osteosarcoma cells. Furthermore, suggest that curcumin has the potential to be a new chemotherapeutic agent in the treatment of osteosarcoma.

Despite the various advantages, the low bioavailability, low solubility, malabsorption by the organism, and instability in the physiological environment, represent a challenge in the use of natural products as medicines. Thanks to advances in nanotechnology, improved nanostructures offer the unique possibility of transport, protection, and delivery of potential therapeutic molecules to specific targets [25]. Furthermore, researchers have directed efforts to design nanostructures composed of one or more components to synthesize a single nanosystem that offers enhanced multifunctional properties capable of aiding tumor treatment and supporting bone formation [26,27]. These systems can be used as nanocarriers allowing the delivery and controlled release of drugs to specific tumor sites, in addition to being able to assist in bone regeneration. This strategy minimizes damage to healthy cells, reduces side effects, and improves therapeutic efficacy [28–30]. There are currently a wide number of potential multifunctional nanomaterials being applied in biomedical research to provide more specific and effective treatment approaches. Among them, hydroxyapatite (HA), which is a calcium phosphate with a chemical composition similar to the chemical composition of the mineral phase of bone tissue, has been widely explored in biological research thanks to its biocompatibility and osteoconductivity [31].

HA has wide use in biomedical materials, such as in the production of scaffolds for tissue engineering [32,33], in the coating of metallic implants [34,35], in drug delivery and controlled release systems [36–38] and in cancer therapy and diagnosis [39–41]. Izadi and colleagues [42] developed a magneto-responsive nanocomposite for chemotherapy delivery. Magnetic particles were integrated into the mesoporous rod-like structures of HA, functionalized with folic acid, which were used for the transport of doxorubicin. The nanocomposite showed aqueous stability and high antitumor efficacy with a magnetically driven release. Ghosh et al. [43] successfully synthesized a nanocomposite of n-HA and polyvinyl alcohol (PVA) polymer for doxorubicin delivery and release. The nanocarrier showed cytotoxicity for MG 63 cells, demonstrating to be a potential anticancer agent in the treatment of osteosarcoma. In an in vitro study, Wang et al. [44] demonstrated that the HA nanorods produced were able to reduce cell viability and inhibit the migration and invasion of OS-732 osteosarcoma cells in healthy tissues. Furthermore, they also demonstrated the efficiency of HA nanorods in suppressing tumor growth in vivo through the downregulation of FAK/PI3K/AKT signaling. HA structures present high stability and flexibility, allowing some transition metal or lanthanide cations to be added as dopants in the apatite crystal lattice [40]. The doping of nano-sized HA with gadolinium as well as the combination with natural anticancer pharmaceutics, are research areas deserving further exploration aiming the use as a theranostic system to promote the diagnosis and treatment of cancer simultaneously [39,45,46]. On the other hand, much attention has been also focused on the synergistic effect of chemotherapeutic drug combinations with natural products such as curcumin hold great promise for enhancing their anticancer efficacy [47–49]. These data will constitute a hallmark and consolidate the next steps of development of those devices, which will include their use as nanotheranostic systems and in vivo applications.

Despite there are currently a considerable number of scientific works describing the study of curcumin loaded hydroxyapatite nanosystems for the treatment of some diseases, the literature still lacks information on curcumin chemical modifications for improving its biological behavior and chemical interaction with hydroxyapatite nanocarrier, aiming desirable features for the treatment of osteosarcoma.

Based on the above, the present work aims to obtain and characterize a nanostructured system consisting of hydroxyapatite nanorods with the potential for the transport of APTS-modified curcumin for the treatment of osteosarcoma. Different techniques were used to characterize the nanoparticles at each step of functionalization, and, together, they corroborate to identify the schematic chemical structures. Few published works describe the curcumin functionalization process by inserting amine groups in the CM structure so that it could interact with nb-HA. The use of APTES in the synthesis of organic-inorganic hybrid

materials acts as a coupling agent for several inorganic substrates. Furthermore, rare of them address the investigation of the structural and energetic properties of the reactions between these molecules using first-principle calculations based on density functional theory (DFT) together with XPS to explore the chemical interactions between CM-APTES and the HA surface. The proposed route of synthesis allows the production of a low-cost and easy-to-obtain nanostructure with good therapeutic potential and the possibility to stimulate bone-guided regeneration in the treated regions, offering multiple benefits.

2. Materials and methods

2.1. Materials

Hexadecyltrimethylammonium bromide (CTAB - $C_{14}H_{42}N.Br$) (Sigma-Aldrich), calcium nitrate, $Ca(NO_3)_2.4H_2O$, (Sigma-Aldrich), dipotassium monohydrogen phosphate, $K_2HPO_4.3H_2O$, (Sigma-Aldrich), sodium hydroxide ammonium (NH3OH), curcumin (Sigma-Aldrich), 3-amino-propyltriethoxysilane - APTES (Sigma-Aldrich), acetic acid P.A. (Neon).

2.2. Synthesis of hydroxyapatite nanorods

The hydroxyapatite nanorods were prepared by the surfactant-assisted hydrothermal method [45]. The present method consisted of the preparation of two precursor solutions: (I) calcium and (II) phosphate. The solution I was produced from the complete dissolution of CTAB in deionized water, to promote the direction of the network through the formation of micelles. Subsequently, the calcium nitrate was solubilized, to obtain a solution with a final concentration of calcium of 0.167 M. The solution was kept under stirring at room temperature. Solution II was obtained by the complete solubilization of dipotassium monohydrogen phosphate, with a final phosphorus concentration of 0.1 M. The pH of both solutions was corrected to 10 with the addition of ammonium hydroxide, and the solution I was added dropwise. The drop to solution II. At the end of the dripping, the suspension was stirred at room temperature for 14 h. The suspension obtained was then transferred to the hydrothermal reactor and led to the hydrothermal treatment at a temperature of 100 °C for 10 h. After the hydrothermal treatment, the suspension was centrifuged, filtered, and washed with deionized water and ethanol. The filtered material remained in an oven at 60 °C for 24 h for drying, and then it was calcined for 6 h at 600 °C. The material obtained was identified as n-HA.

2.3. Modification of curcumin with APTES

The modification of CM with APTES was developed based on the work of Hamed et al. [50] with minor changes. The modification of CM with APTES was carried out from the complete solubilization of 1 mM of CM in 98% acetic acid with the subsequent addition of 4 mM of APTES. The mixture was stirred for 24 h at 75 °C in an inert atmosphere under a reflux system. After the end of the reaction, the mixture was dried in an oven at 60 °C for 24 h. The material was then suspended in deionized water and lyophilized to obtain the powder sample. The sample obtained in this process was identified as CMAP.

2.4. Obtaining the nanostructures of n-HA and CMAP

The incorporation of CMAP into n-HA was carried out directly by mixing CMAP and n-HA, with a mass ratio of 1:1 in 50 ml of deionized water. The mixture was kept under vigorous stirring for 24 h at 50 °C. The resulting orange powder was collected under vacuum filtration and washed with deionized water and excess ethanol to remove unreacted CMAP. Subsequently, the material was dried in an oven at 60 °C for 24 h. The obtained nanostructure was identified as CMAP-HA.

2.5. DFT simulations

First-principle calculations based on Density Functional Theory (DFT) [51,52] and TD-DFT [53] were performed on Amsterdam Modelling Suite (AMS) package [54]. The absorption calculations were performed using the hybrid B3LYP [55] exchange-correlation (xc) functional including 20% of Hartree-Fock (HF) exchange and the TZP basis set considering 50 excited states. The UV–Vis spectra were convoluted with Gaussian functions having 60 nm of half-width at half-maximum (HWHM). Ethanol implicit solvation effects were carried out using the COSMO (Conductor-like Screening model) [56–59] considering the Allinger atomic radii [60]. The vibrational normal modes and frequencies were calculated using B3LYP/TZP in the gas phase to confirm an energy minimum and to analyse the Gibbs free energy of the proposed reactions. The variation of the Gibbs free energy (ΔG) of possible reactions leading to curcumin/APTES complexes is the difference between the calculated Gibbs energy of products ($\Delta G_{products}$) and reactants ($\Delta G_{reactants}$), that is, $\Delta G = \Delta G_{products}$-$\Delta G_{reactants}$. All calculations were employed using Becke 3 (good) [61] for geometry optimization and UV–Vis spectra with an SCF convergence criterion of 10^{-6}, without symmetry constraints.

2.6. Characterizations

DFT calculations were used to investigate the energetic properties of the reactions between curcumin and APTES. The structural configuration of all molecules used in this study is described in the DFT investigation Results section. The crystalline phases of the sample were evaluated by X-ray diffraction (XRD - Rigaku Inc., Japan) with Cu Kα radiation ($\lambda = 0.154$ nm) in which data were collected from 10° to 80° (2θ) with a size of 0.4°/min step to perform Rietveld refinement using FullProf Suite adopting the Crystallography Information File number 16742 from ICSD (Inorganic Crystal Structure Database). The morphologies of the synthesized materials were evaluated by the images obtained by transmission electron microscopy using the Tecnai G2-12 – Spirit Biotwin FEI - 120 kV equipment from the Microscopy Center of the Federal University of Minas Gerais (UFMG). The samples were dispersed in ethanol and sonicated for 10 min in an ultrasound bath. After decanting for 10 min, a drop of the suspension was deposited on a 200 *mesh* carbon-coated copper support grid. Fourier Transform Infrared Spectroscopy (FTIR) was performed to investigate the functional groups characteristic of the synthesized samples. Infrared spectra in the wavelength range of 4000 - 400 cm^{-1} were obtained by the Nicolet 6700 spectrophotometer (Thermo Scientific, USA), with a resolution of 4 cm^{-1} to 64 scans.min^{-1}, with samples prepared in pellets of potassium bromide (KBr). Thermogravimetric analysis (TGA) was performed on a DTG-60H analyzer (Shimadzu, Japan) at 25–800 °C with a heating rate of 10 °C min^{-1}. Measurements were performed in a nitrogen atmosphere with a flow rate of 100 ml min^{-1}. Differential Scanning Calorimetry (DSC) was used to assess the interaction of MC with APTES. The analysis was performed on the DSC 60 equipment (Shimadzu, Japan). The test was carried out in hermetically sealed aluminium sample holders, with a heating rate of 10 °C.min^{-1} in the temperature range of 25 °C to 450 °C, with an N_2 flow of 100 ml min^{-1}. The UV–Visible Spectroscopy (UV-VIS) technique was used to identify curcumin in the CMAP-HA sample. For the test, the samples were dispersed in 70% ethanol solution (v/v) with the aid of an ultrasound bath for 10 min. The assay was performed on the UV-2550 spectrophotometer (Shimadzu, Japan). Zeta potential analysis was performed using the Nanozetasizer Zs equipment (Malvern Instruments, United Kingdom). The measurements were carried out at a temperature of 25 °C. For analysis, samples were dispersed in Milli-Q® water at a concentration of 0.05 mg ml^{-1} in a tip ultrasound with an energy of 10 kJ. The investigation of the surface chemical composition of the samples was performed by X-ray Photoelectron Spectroscopy (XPS). Measurements were conducted using monochromatic Al Kα X-ray (E = 1486.6 eV) radiation and a Phoibos 150 electron energy analyzer

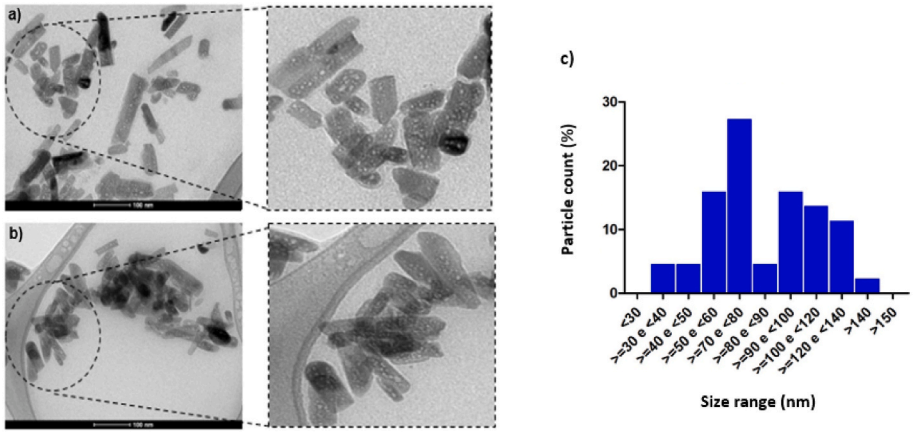

Fig. 1. Micrograph of a) n-HA, b) CMAP-HA samples, and c) Distribution of the size range of hydroxyapatite nanorods.

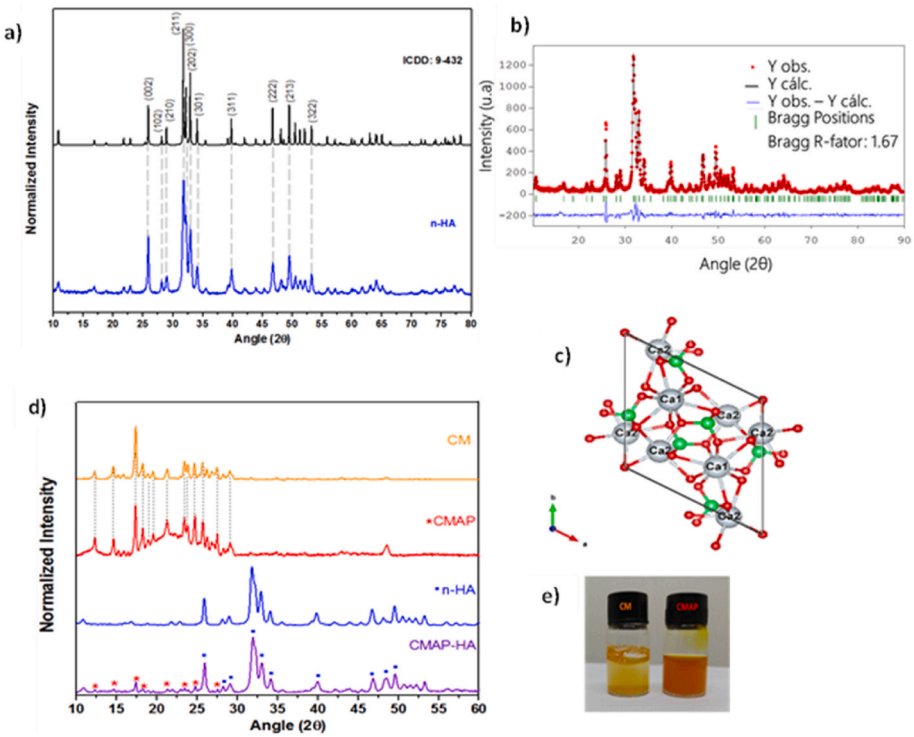

Fig. 2. a) Diffractogram of the n-HA sample; b) Rietveld refinement of the synthesized n-HA sample compared to the hydroxyapatite standard; c) Schematic of the synthesized nb-HA unit cell obtained from the Rietveld refinement; d) Diffractogram of CM, CMAP, n-HA, and CMAP-HA samples; e) photo showing the difference in dispersibility of CM and CMAP samples in water.

(Specs GmbH) in ultra-high vacuum equipment. To prevent eventual charge effects, the binding energy scales were corrected, taking the C 1s peak (at 284.6 eV) as a reference. The analyses were carried out with the samples deposited on conductive tape on a stainless-steel sample holder.

2.7. Cells and cell culture

U2OS cells from the primary malignant bone tumor and primary human fibroblasts (HDFa) were obtained from (ATCC, Manassas, VA, and Life Technologies, Inc.). The cells were cultured at 37 °C in 5% CO2 in Dulbecco's modified Eagle's medium; DMEM (Life Technologies, Inc.) containing 10% fetal bovine serum, 1 mm sodium pyruvate, 100 units. ml^{-1} penicillin, and 100 μg ml^{-1} streptomycin (Life Technologies, Inc.).

2.8. Cell viability and cell proliferation assays

Cell viability was measured using MTT (3- (4,5-dimethylthiazol-2-yl)-2,5-diphenyl tetrazolium bromide) and cell proliferation assay investigated the n-HA and curcumin nanorods biocompatibility [62,63]. For the MTT assay, U2OS and HDFa cells were seeded (2.0 × 104 cells/well) on 96 well plates. After 24 h incubation (37 °C, 95% humidity, and 5% CO_2), cells were treated with the materials in four concentrations (5, 10, 50, and 100 μg ml^{-1}). Experiments were performed in triplicate, including 3 blank and 3 non-treated control wells. After another 24 h incubation, the medium was removed and washed with phosphate-buffered saline (PBS). Next, 10 μl of MTT solution (5 mg ml^{-1}) and 90 μl of DMEM were added per well. The plates were incubated for 3 h until the formazan crystallization and the formazan salts were dissolved with sodium dodecyl sulfate-10% HCl solution. The

Table 1
Crystallographic structural parameters a, b, c, and unit cell volume (V) of the n-HA synthesized sample.

Sample	V (Å^3) ± SD	a (Å) ± SD	b (Å) ± SD	c (Å) ± SD
Standard (ICSD 16742)	530.1390	9.43200	9.43200	6.88100
n-HA	530.5433 (±0.049)	9.42950 (±0.48.10^{-3})	9,42950 (±0.48.10^{-3})	6.88990 (±0.39.10^{-3})

Table 2
Zeta potential measurements of n-HA, CMAP, and CMAP-HA samples.

Samples	Zeta Potential (mv) ±SD
n-HA	−18.47 ± 2.38
CMAP	+38.48 ± 1.91
CMAP-HA	+15.3 ± 0.77

absorbance was measured at 570 nm using a Multiskan GO microplate reader (Thermo Scientific, USA). The absorbance from blank wells was subtracted from each measurement and the cell viability was calculated as a function of the control group absorbance.

For cell counting, U2OS and HDFa cells were seeded (1.0 × 105 cells/well) on 24 well plates. After 24 h of incubation, cells were treated with materials in the following concentrations 10, 50, and 100 μg ml^{-1}. Next cells were incubated for 20 min with Calcein red-orange AM (2.5 μM/well) and 1.0 μM/well of Hoechst 33342 (Thermo Scientific, USA). The images were taken at random representative areas of each well using an inverted fluorescence microscope EVOS-FL (Thermo Scientific, USA); 10 images per group. Experiments were performed in triplicate with 3 positive controls. The viable cell counting to access cell proliferation was performed using the ImageJ software (https://imagej.nih.gov/ij/).

2.9. Statistical analysis

Results are presented as mean ± SEM. Data were analyzed using GraphPad Prism 9 and Microsoft Excel. Differences between experimental groups were assessed for significance using a One-way anova analysis of variance. Statistical significance was defined as $p < 0.05$.

3. Results and discussions

3.1. Transmission electron microscopy - TEM

The morphological characterization of the nanoparticles was performed by the TEM technique and the images obtained are shown in Fig. 1 (a) for n-HA and (b) for CMAP-HA.

It could be observed that both samples have the shape of nanorods of non-uniform sizes. In the image (b), referring to the CMAP-HA sample, it was not possible to observe any significant changes that could be associated with the presence of CMAP.

The size distribution (Fig. 1c) of particulate hydroxyapatite nanorods ranged from 30 to 140 nm with an average value of 90.2 nm, and a size concentration centered around 70–80 nm, very close to the average presented. All measurements were performed using the Quantikov Analyzer software [64].

3.2. X-ray diffraction (XRD)

The crystalline phases present on hydroxyapatite nanoparticles (n-HA) were investigated through an x-ray diffraction technique (Fig. 2a). The diffractogram of the synthesized sample was compared with the file 9–432 of the PDF (Powder Diffraction File) database of the International Center for Diffraction Data (ICDD), revealing only the crystalline phase of hydroxyapatite with a hexagonal arrangement and space group P63/m, with no other crystalline or amorphous phases identified within the limit of detection of the technique. The characteristic peaks at Bragg angles of approximately 32°, 33°, and 34° (2θ) can be attributed to the reflections of the planes (211), (300), and (202) respectively, according to the literature [46].

The lattice parameters of the hydroxyapatite structure were investigated by performing the Rietveld refinement method, and the results are presented in Table 1 and Fig. 2b which show good agreement with the reference values (ICSD16742). The discrete increments in parameter C and in the unit cell volume, as well as the short contractions in the unit cell a and b dimensions, can be a result of a carbonate substitution at phosphate sites. According to Madupalli et al. [65], these observations are characteristic changes of type B carbonated hydroxyapatite. The n-HA had a Ca/P ratio of 1.62, confirmed by X-ray fluorescence spectroscopy (Table S1, Supporting Information), which is close to the value of stoichiometric hydroxyapatite, which is 1.67 [66]. This difference can be explained by calcium deficiency, possibly caused by the replacement of phosphate ions with carbonate ions [67]. These findings will be further discussed in the FTIR section. Fig. 2c shows the synthesized n-HA unit cell, obtained from the Rietveld refinement.

According to Fig. 2d, CM exhibited characteristic XRD peaks at 12.28°, 14.6°, 17.36°, 18.22°, 21.28°, 23.42°, 25.68° and 29.06° Bragg angles revealing the crystalline profile of this molecule in agreement with the literature [55], while the CMAP diffractogram exhibited a diffuse halo approximately from 18° to 30° 2θ range that is characteristic of short-range periodicity or amorphous phases such as silicates [68]. This change may indicate the presence of APTES that generally forms amorphous structures. However, as the presence of CM peaks still exists, this suggests that only a small portion of APTES interacted with CM but still may be responsible for the improvement in the CM water dispersibility as shown in the photographs inserted in Fig. 2e. These photographs show the differences in dispersion in water of the CM and CMAP samples, both with the same concentration. Comparing the diffractogram of the CMAP-HA sample with those of the CMAP and n-HA samples, it is possible to observe the presence of the characteristic peaks of hydroxyapatite and discreet signs of the CMAP peaks. This low intensity of CMPA peaks may be related to the small amount of CMAP present in the CMAP-HA sample, which is mainly constituted by n-HA.

3.3. Zeta potential - ζ

Zeta potential plays an essential role in understanding the state of particle surface properties. It not only determines the stability of the particles used in studying surface charges anchored in nanoparticles but also defines the possible interaction of nanoparticles with different types of plasma membranes [69]. Table 2 presents the values of the zeta potential measurements of the n-HA, CMAP, and CMAP-HA samples.

The negative surface charge of the n-HA sample is attributed to the presence of OH^- groups, which ionize to O^{-2} and H^+ in aqueous dispersion at neutral pH. On the other hand, the results showed that CMAP presented a high positive charge zeta potential thanks to the presence of the NH_3^+ group, due to the protonation of the amine group present in APTES. This positive charge suggests more excellent stability, since suspensions with zeta potential values greater than +30.0 mV and less than −30 mV are considered stable [70]. The CMAP-HA sample showed a reduction in the zeta potential value when compared to the CMAP. This result can be attributed to the presence of n-HA, which contributes a negative charge due to the presence of the ionizable hydroxy (OH^-) group.

The changes in the zeta potential values of the samples are a strong indication of a successful surface modification, indicating that the proposed reactions with CM and APTES took place and that the final molecule was successfully incorporated into the HA nanoparticles.

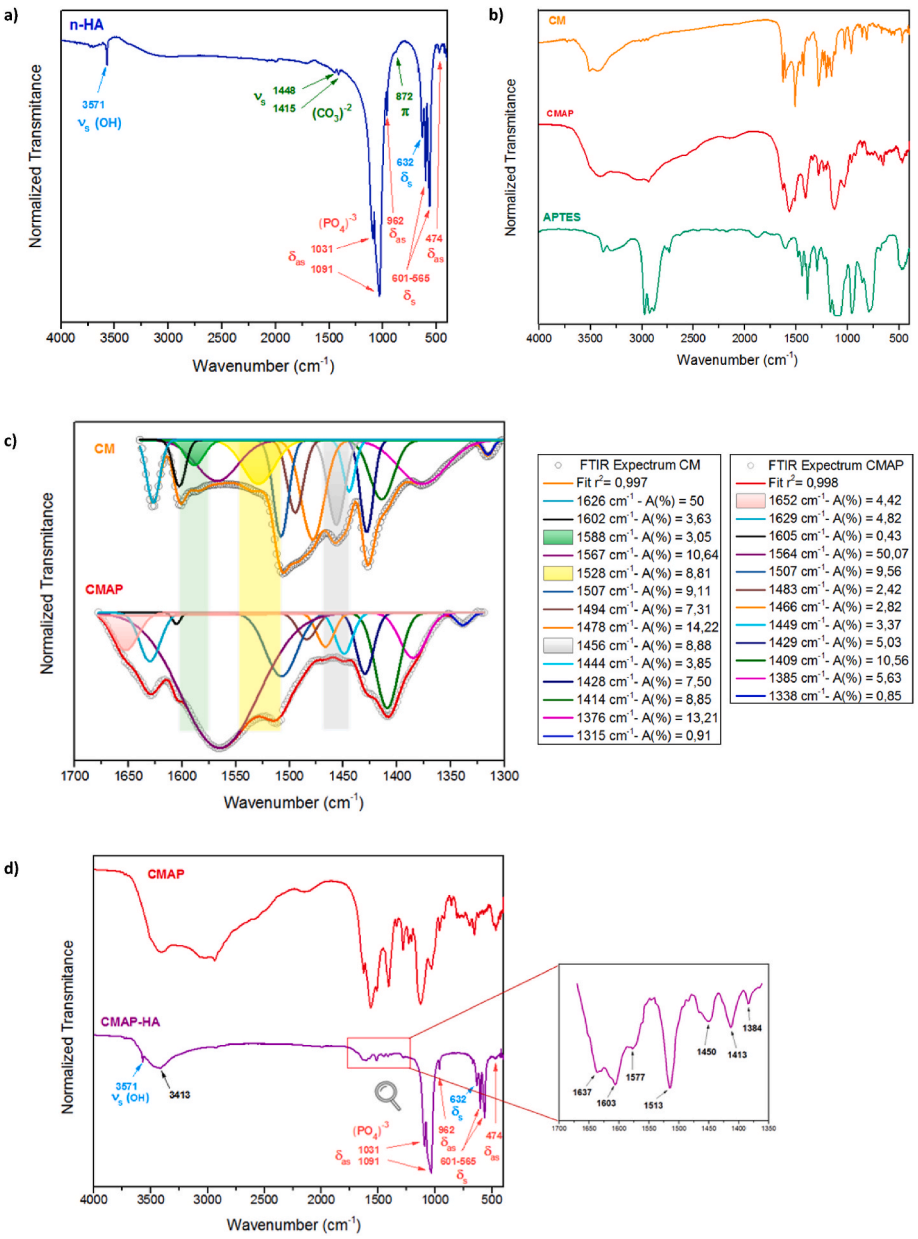

Fig. 3. FTIR spectra of a) n-HA sample b) CM, APTES, and CMAP; c) Deconvolution of the FTIR spectra of the CM and CMAP samples; d) Comparative analysis of FTIR spectra of CMAP and CMAP-HA samples.

Several articles report that positively charged nanoparticles are more easily uptake by the cells than the other nanoparticles due to the attractive interaction between positively charged nanoparticles and the negative cell membranes [71–73]. However, some authors consider this interaction privileged, due to the favorable electrostatic interaction, a reductionist theory for not taking into account other characteristics of the nanoparticle in a biological medium, in particular the corona protein [74,75]. The formation of the corona protein occurs when the nanoparticle is introduced into a biological medium, where it is quickly covered by proteins that adsorb on its surface. This so-called protein crown changes the original physicochemical characteristics of the nanoparticle and generates a new interface that defines the "biological identity" of the nanoparticle [74,75]. In addition, studies reveal that nanoparticles with a negative surface charge show greater cellular internalization in cancer cells [76]. In another work, Naqshbandi and Rahman [77] reported that the negative zeta potential favours the fixation and proliferation of bone cells by increasing the adsorption of Ca^{2+} ions since the binding of such cells is dependent on the adsorption of ions Ca^{2+}.

3.4. Fourier transform infrared spectroscopy - FTIR

The chemical analysis performed through the FTIR technique evidenced the main characteristic transmittance bands of hydroxyapatite vibrational modes on the spectrum of the n-HA sample (Fig. 3), as previously reported in the literature [45,46,78]. The bands at 3572 cm^{-1} and 632 cm^{-1} correspond, respectively, to axial and angular symmetrical deformations of hydroxyl groups in hydroxyapatite structure, while the wideband from 3500 to 3000 cm^{-1} is attributed to the vibrational mode of hydroxyl groups from water adsorbed in the crystal lattice [79,80]. The bands assigned to the vibrational modes of phosphate groups are observed at 1091, 1031, 962, 601, 565, and 474 cm^{-1}. The main signal of the phosphate group appears in the triple degenerate domain, located at 1091 cm^{-1} and 1031 cm^{-1}, which represents the vibration of asymmetric axial deformation of the P–O bond of the $(PO_4)^{-3}$ group. The non-degenerate band at 962 cm^{-1} is attributed to symmetrical axial

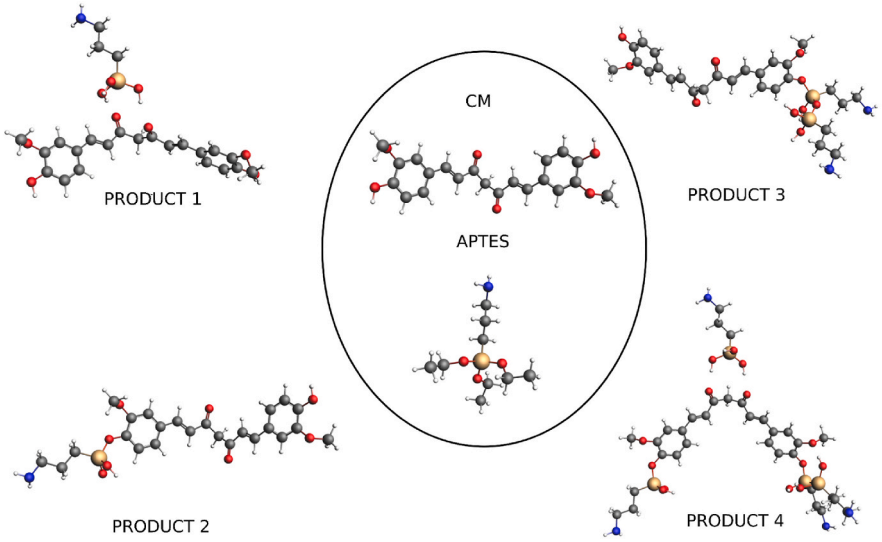

Fig. 4. Curcumin (CM)/APTES complexes. Product1: an APTES fragment interacting with CM via hydrogen bonds. Product2: an APTES fragment replaces a hydroxyl group. Product 3: two APTES fragments replace a hydroxyl group. Product 4: two APTES fragments replace two hydroxyl groups, and an APTES fragment binds via hydrogen bonds.

Table 3
Proposed reactions and the variation of Gibbs free energy. CM and APTES are abbreviations for curcumin ($C_{21}H_{20}O_6$) and (3-Aminopropyl) triethoxysilane ($C_9H_{23}NO_3Si$), respectively. Product 1, Product 2, Product 3, and Product 4 are the CM/APTES complexes shown in Fig. 4.

Reaction	ΔG (eV)
CM + APTES ⟶ Product 1 + $3C_2H_4$	0.11
CM + APTES ⟶ Product 1 + C_6H_6 + $3H_2$	−0.42
CM + APTES ⟶ Product 2 + $3C_2H_4$ + H2O	0.17
CM + APTES ⟶ Product 2 + C_6H_6 + $3H_2$ + H_2O	−0.36
CM + 2 APTES ⟶ Product 3 + $6C_2H_4$ + $3H_2O$	−0.16
CM + 2 APTES ⟶ Product 3 + $2C_6H_6$ + $2H_2O$ + $6H_2$	−1.22
CM + 4 APTES ⟶ Product 4 + $12C_2H_4$ + $3H_2O$	0.11
CM + 4 APTES ⟶ Product 4 + $4C_6H_6$ + $3H_2O$ + $12H_2$	−2.01

deformation of the P–O bond [70,81,82]. The triple degenerate vibrational mode associated with symmetrical angular deformation of the P–O–P bond is located at 601 cm^{-1} and 565 cm^{-1}. The small band at 474 cm^{-1} is attributed to the doubly degenerate vibrational mode of the asymmetric angular deformation of the P–O–P bond [83,84]. In addition, the doubly degenerate vibrational mode of the symmetric axial deformation of $(CO_3)^{-2}$ is observed at 1448 and 1415 cm^{-1}, as well as the carbonate vibrational mode of the out of plane angular deformation at 877 cm^{-1} [85]. According to Madupalli et al. [65], the presence of these bands suggests the obtaining of type B carbonated HA, in which the carbonate replaced phosphate groups at anionic sites in the hydroxyapatite structure. This substitution likely occurred due to the absorption of atmospheric CO_2 during the synthesis or after the end of the calcination process, since the cooling is not carried out in an inert atmosphere [45,46]. Also, according to the authors, the carbonate present in the mineral phase of bone tissue is, for the most part, type B, which increases the chemical similarity of the synthesized HA with the biological one.

Fig. 3b shows the CM, APTES, and CMAP spectra for comparison purposes. Detailed identification of the functional groups in the FTIR spectra of the CM and APTES is presented in the Supporting Information, Fig. S1. It was possible to observe the change in the shape and position of some bands of the CMAP spectrum. These changes may indicate the interaction of the CM with APTES. To determine these changes, the deconvolution of the CM and CMAP spectrum was performed in the region from 1700 to 1300 cm^{-1} and shown in Fig. 3c, and in Table S2 the values of both the displacement of the bands and their respective areas are listed.

Practically all CMAP bands were shifted to higher or lower wavenumbers compared to CM values. In particular, attention is drawn to the CM bands located at 1588, 1528, and 1456 cm^{-1}, which are not present in the CMAP spectrum. These bands are attributed to the axial deformation of the C═O and C═C bonds from the aromatic ring [86]. In addition, the band at 1652 cm^{-1} is also highlighted, present only in the CMAP spectrum. According to Oliveira et al. [87], this band can be attributed to the axial deformation of the C═C bond of the aromatic ring. Because of all these observations, it is possible to consider that these changes related to the vibrations of the C═C bond of the aromatic ring are the result of the interaction with APTES. In theory, the hydrogen bond of the silanol group of APTES with the oxygen of the phenol group of curcumin would cause a deformation in the aromatic ring, generating changes in the vibrations of its structure, which would justify the emergence of this new band. However, the disappearance of bands at 1588, 1528, and 1456 cm^{-1} could also be related to the deformation caused in the ring. In addition, all bands had their area (A%) changed. In particular, the band located at 1567 cm^{-1} in the CM sample, which underwent a small shift to 1564 cm^{-1} in the spectrum of the CMAP sample, had an increase of more than 42%. This significant increase may be related to the overlapping of the vibrational modes of the C═O bonds and the amine group.

In the spectrum of CMAP-HA, Fig. 3d, it is possible to observe the main bands of the phosphate group from n-HA. In addition, it is also possible to observe the presence of characteristic CMAP bands. Generally, the bands are related to the vibrational modes of the C═O, C═C bonds of the aromatic ring and alkene, and the C–O bond of the phenol group. The existence of these bands confirms the presence of the CMAP molecule in the hydroxyapatite nanorods. It is also possible to verify the presence of the band located at 3571 cm^{-1} attributed to the free hydroxyl of n-HA, which can be considered an indication that not all hydroxyls interacted with the amine group of CMAP. The concomitant presence of the band at 3413 cm^{-1} confirms this hypothesis since it is attributed to intermolecular hydrogen bonding.

3.5. DFT simulation

DFT calculations on possible curcumin/APTES complexes may shed light on questions regarding the atomic structures of the obtained

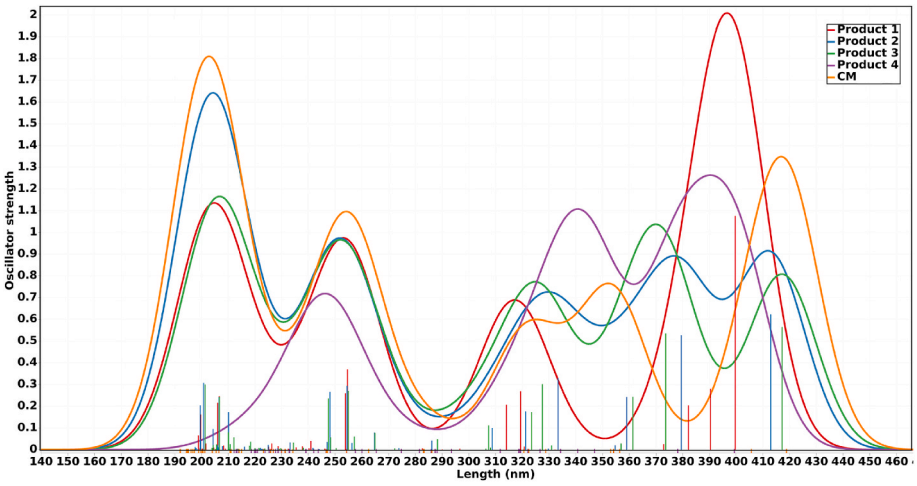

Fig. 5. Theoretical absorption spectra for 50 excited states obtained from a full TDDFT/B3LYP-TZP/Ethanol.

Table 4
Orbital Energies and HOMO-LUMO (H-L) gap (eV) calculated with DFT. Optical gap (eV and nm), the state responsible for the first absorption band, oscillator strength (f_{osc}), and main orbitals in the electronic transition calculated with full TDDFT.

Products	HOMO (eV)	LUMO (eV)	H-L gap (eV)	Optical gap (eV)	Absorption (nm)	State	f_{osc}	Orbitals
Product1	−6.01	−2.43	3.58	3.10	399.62	1st	1.07	HOMO-LUMO+1 (15%) HOMO-1-LUMO (82%)
Product2	−5.99	−2.51	3.48	3.00	412.92	1st	0.63	HOMO-LUMO (96%)
Product3	−5.99	−2.57	2.97	2.97	417.20	1st	0.56	HOMO-LUMO (97%)
Product4	−6.33	−2.55	3.61	3.10	399.37	1st	0.65	HOMO-LUMO (92%)
CM	−5.97	−2.51	3.46	2.96	418.84	1st	0.81	HOMO-LUMO (97%)

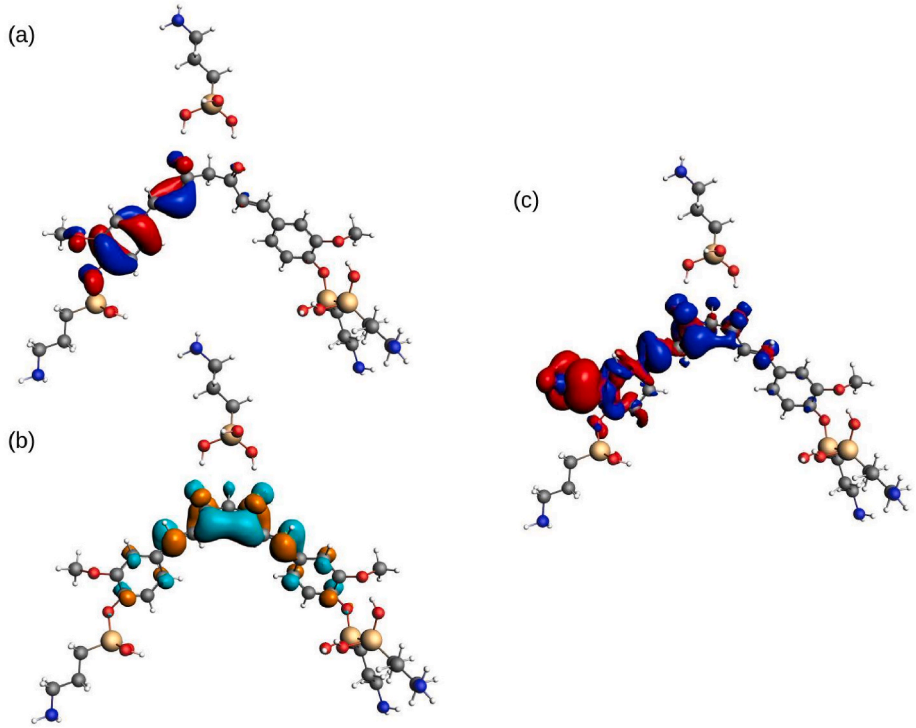

Fig. 6. Main molecular orbital plots for Product 4. (a) HOMO, (b) LUMO, and (c) Difference density for the first excited state. The colour difference on the frontier orbitals means different signs, and in the excited state, it shows that the electron goes from red to blue. (For interpretation of the references to colour in this figure legend, the reader is referred to the Web version of this article.)

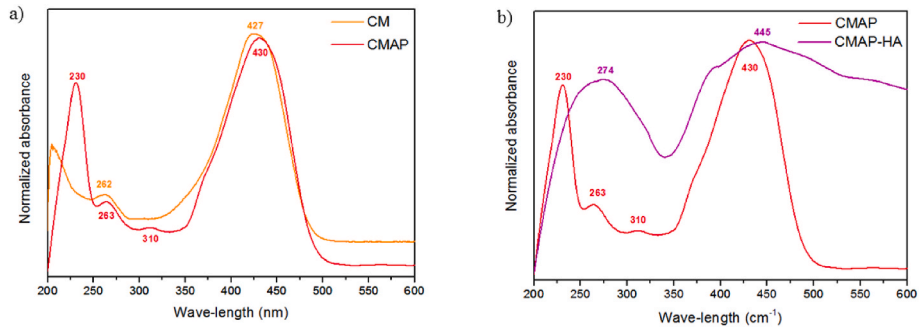

Fig. 7. –UV-Vis spectra of a) CM and CMAP samples, and b) CMAP and CMAP-HA samples.

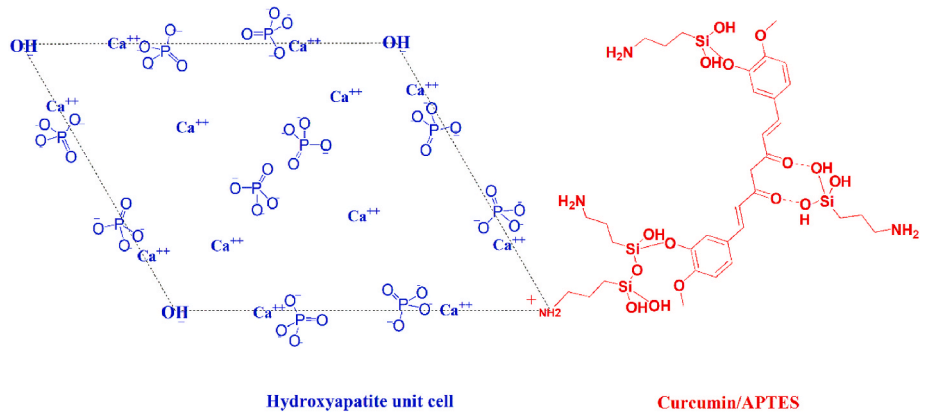

Scheme 1. Possible curcumin/APTES interaction with hydroxyapatite unit cell through substitution of HA hydroxyls for protonated amine group from APTES moiety of curcumin/APTES molecule.

compounds. Based on the experimental results presented, we propose curcumin/APTES complexes in which APTES molecules bind to curcumin keto configuration via hydrogen bonds or replace one or both hydroxyl functional groups of the curcumin molecule, Fig. 4. The variation of the Gibbs free energy of possible reactions leading to those structures indicates whether curcumin/APTES complexes form spontaneously from APTES and curcumin molecules in a carboxylic acid environment. Table 3 shows the proposed reactions and the variations of the Gibbs free energy (ΔG) between reactants and products. For each curcumin/APTES complex (Product 1, Product 2, Product 3, and Product 4), it was considered two reactions that differ in the products formed. One can see in Table 3 that almost all the proposed reactions are spontaneous (negative values of ΔG indicate spontaneous reactions). The overall trend is that ΔG decreases as the number of APTES fragment binding to the curcumin molecule increase, indicating that the structure Product 4, shown in Fig. 4, is the most energetically favorable to occur among the proposed ones.

In order to explore the theoretical photophysical properties, we performed calculations based on DFT and TDDFT formalism to determine UV–Vis spectra (see Methodology). The absorption spectra calculated with the COSMO solvation model for the four curcumin/APTES complexes (Product1,2,3,4) in comparison with curcumin are presented in Fig. 5. The HOMO (Highest Occupied Molecular Orbital) and LUMO (Lowest Unoccupied Molecular Orbital) energies, the optical gap, oscillator strength (f_{osc}), and the orbitals involved in the first absorption peak are presented in Table 4. First, the CM theoretical spectrum shows absorption at 418 nm in great agreement with the experiments, in Fig. 7 [88–91]. This first peak has a contribution of 97% HOMO (π)-LUMO (π*) transition, as we can see in Fig. S2 and Table 4. The optimized molecular structure of curcumin in the keto configuration exhibits a bend of approximately 111.1°. LUMO Orbital is mainly located in the middle of the bend with bonding orbitals, while the feruloyl group has antibonding orbitals. HOMO orbital is mostly composed of bonding orbitals (See Fig. S2) [89]. In comparison with the experimental spectra presented in Fig. 7, the complex curcumin/APTES (CMAP) has a similar absorption spectrum compared with CM with an additional band in smaller wavelengths. Furthermore, the CMAP spectrum shows a small shift concerning the CM spectrum for the band between 400 and 500 nm. The theoretically proposed complex also presents a similar behavior. The spectra of the Product1 and Product4 complexes have a shift of the order of 19 nm with respect to the CM, while Product 2 and 3 have a shift of less than 6.0 nm. Product1 has the largest shift compared with CM, with the (HOMO-1/LUMO) transition being the most important contribution to the transition to the first excited state. Fig. S3, in the Supplementary Information, presents the main molecular orbitals (MO) of these transitions. Product 2, Product 3 (both in Fig. S4), and Product 4 (Fig. 6) have an absorption mostly HOMO to LUMO for the transition to the first excited state. Because the complexes conserve much of the CM geometry, the molecular orbitals involved in electronic transitions in the first excited state are similar. In the Product 2 and Product 3 complexes, because of the replacement with the APTES fragment, the HOMO orbital is concentrated only on the unaltered side. It is interesting to note the small changes in the values of HOMO and LUMO energies and the H-L gap presented in Table 4. It is possible to see that both the substitution of the hydroxyl group by the APTES fragment and its interaction via hydrogen bonds do not considerably alter these values. The same happens when we observe the optical gap calculated via TDDFT. This may probably be the reason why, in Fig. 7, there is no considerable shift in the CMAP spectrum concerning the CM.

Since the functionalization process of HA nanoparticles with curcumin/APTES carried on a slightly acidic medium, an interaction between protonated amine groups from APTES moiety of the functionalizing molecule and the hydroxyapatite unit cell can occur from substitution in hydroxyl sites (Scheme 1), as suggested by Cipreste and colleagues when

Table 5
Analysis of mass loss of CM, APTES, and CMAP samples.

Temperature Range (°C)	Weight loss (%)				
	CM	APTES	CMAP	n-HA	CMAP-HA
25–150	0.35	86.74	13.00	0.52	1.13
150–250	0.68	13.26	13.90	0.97	0.94
250–500	58.59	0	19.00	0.56	5.84
500–800	31.90	0	21.60	0.02	1.45

these authors studied the functionalization of hydroxyapatite nanoparticles with aminated folic acid [39].

3.6. UV–Vis spectroscopy

In order to verify the presence of CM in the samples of CMAP-HA and CMAP-HA nanocomposites, the UV-VIS assay was performed, and the results are shown in Fig. 7.

According to the literature, CM absorbs in the visible region with a maximum ranging from 410 to 430 nm, due to the excitation of the π→π* transition electron [17,18]. The CMAP sample showed a maximum absorption band at 430 nm, presenting a second band with significant intensity at 230, and two much smaller ones at 310 nm and 263 nm, Fig. 7a. In addition, CMAP disperses much better in water than pure CM. Fig. 2e presents the photo showing the difference in the dispersibility between the CM and CMAP samples.

The above observations reveal that the CMAP spectrum is distinct only in a part of the CM spectrum. This indicates that a chemical interaction between APTES and CM may have occurred. However, the existence of the band at 430 nm indicates that there is still pure CM. This indicates that part of the CM did not interact with APTES; however, the amount that interacted was enough to improve its dispersibility in water.

Fig. 7b shows the spectra of CMAP and CMAP-HA. The spectrum of the CMAP-HA sample showed maximum absorbance at 445 nm, confirming the presence of CMAP in the HA nanoparticles. The main differences observed were the widening and displacement of the bands. The broadening of the bands may have occurred due to the presence of hydroxyapatite, resulting in a non-uniform dispersion with particles of different sizes, causing light scattering. Furthermore, it is also possible to observe that the bands at 310 nm and 230 nm disappeared, possibly due to the broadening of the band with a shift to 274 nm.

3.7. Thermal analysis (TG and DSC)

The thermal stability of nanocomposites and n-HA were evaluated by thermogravimetric analysis, and the results are shown in Table 5 and Fig. 8.

In Fig. 8a, in the DTG curve, it is possible to observe that the degradation of CM occurs in two steps and starts at approximately 120 °C and extends to 330 °C. The second stage goes up to 800 °C without completely degrading the CM, leaving a residue corresponding to 9.2% by mass. The mass losses in the respective stages were 22.90% in the first stage and 67.90% in the second stage. In a study carried out by Chen et al. [92], they suggest that step I of CM degradation is due to the decomposition of the substituent groups of curcumin and step II due to the decomposition of the two benzene rings of CM. curcumin.

APTES shows rapid degradation in a single step, around 150 °C,

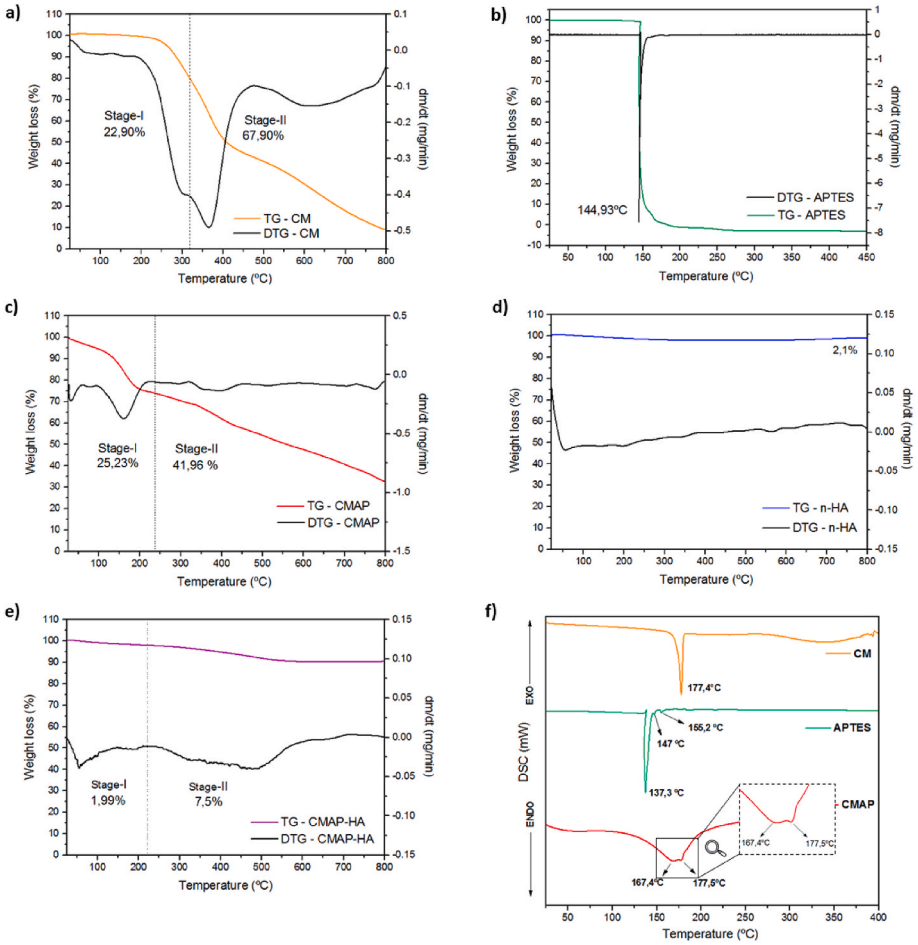

Fig. 8. a) Thermogravimetric curve of the CM, APTES, CMAP, nb-HA, and CMAP-HA samples; b) DSC curves of CM, APTES, and CMAP samples.

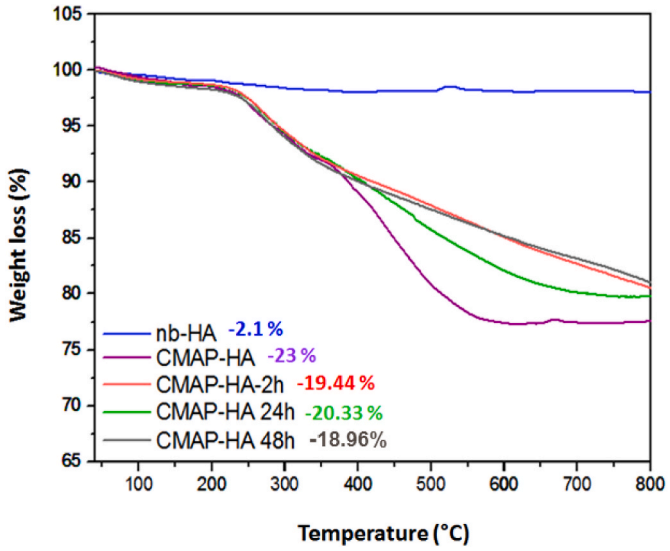

Fig. 9. Mass loss of CMAP-HA samples to the stability test carried out in SBF solution.

confirmed by the derivative of the thermogravimetry curve. The CMAP, in turn, has a profile more similar to the CM, with slower rates and steps that start at lower temperature ranges. The mass loss related to the first stage is close to that of the CM, however the second is approximately 20% lower. In addition, the percentage of residue is higher, which may indicate that the material is more stable and only degrades completely at higher temperatures.

Analyzing the mass losses by TG, the degradation of CM occurs slowly up to a temperature of 250 °C. In contrast, APTES degrades completely up to a temperature of 250 °C. Unlike CM and APTES, CMAP showed an almost proportional loss of mass until the temperature of 250 °C. However, its mass loss in the range of 25–150 °C is higher when compared to CM and much lower when compared to APTES. In the range of 250–500 °C, where the greatest mass loss of CM occurs, CMAP presents a mass loss of less than half of the mass loss of CM. This mass loss profile suggests greater CM stability with APTES due to a possible interaction between the two and can be considered an indication of the effectiveness of the functionalization.

It is possible to observe a small mass loss of the n-HA sample compared to the CMAP-HA sample. As n-HA is a ceramic material, high

Table 6
Surface chemical composition measured by XPS.

Sample	Electronic Level	Binding energy (eV)	AT (%)
CM	O 1s	532.6	20.2
	C 1s	284.6	79.8
CMAP	O 1s	531.6	22.9
	C 1s	284.6	57.4
	N 1s	399.6	8.2
	Si 2p	102.6	11.6
CMAP-HA	O 1s	529.9	31.1
	C 1s	284.4	50.5
	N 1s	397.4	0.8
	F 1s	687.4	1.0
	Ca 2p	348.4	7.5
	P 2p	132.4	6.7
	Si 2p	101.4	2.4

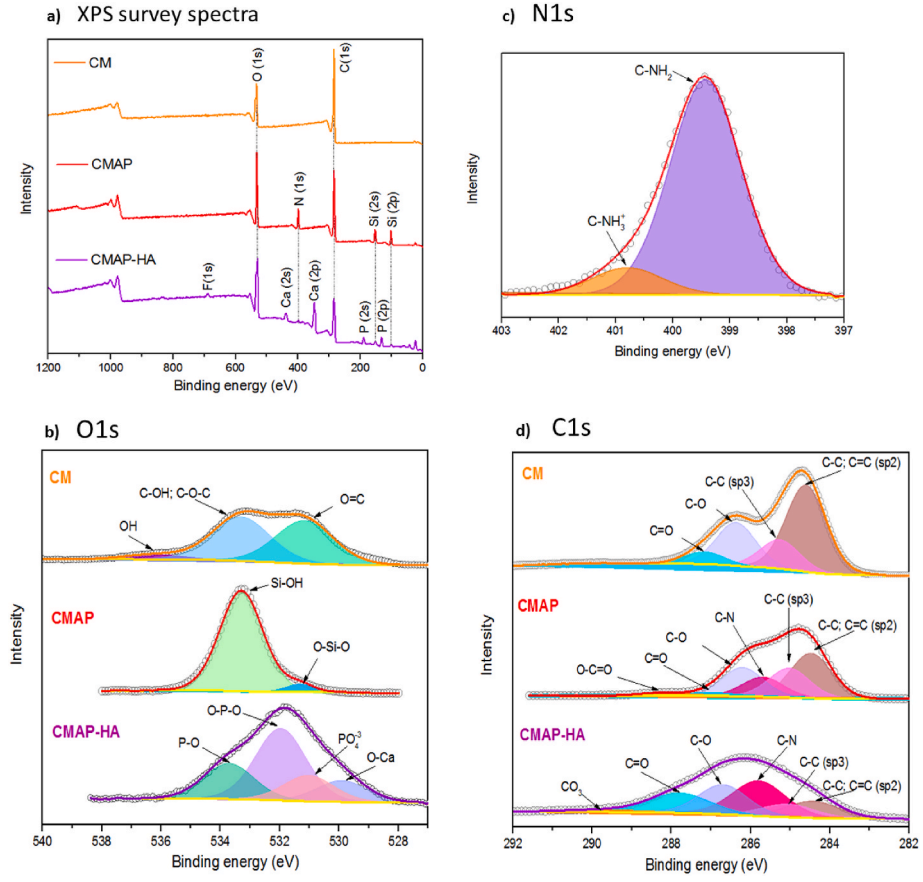

Fig. 10. (a) XPS survey spectra for samples CM, CMAP, and CMAP-HA High-resolution XPS spectra of (b) O 1s, for CM, CMAP, and CMAP-HA samples; (c) N 1s for the CMAP sample; and (d) C 1s for the CM, CMAP, and CMAP-HA samples.

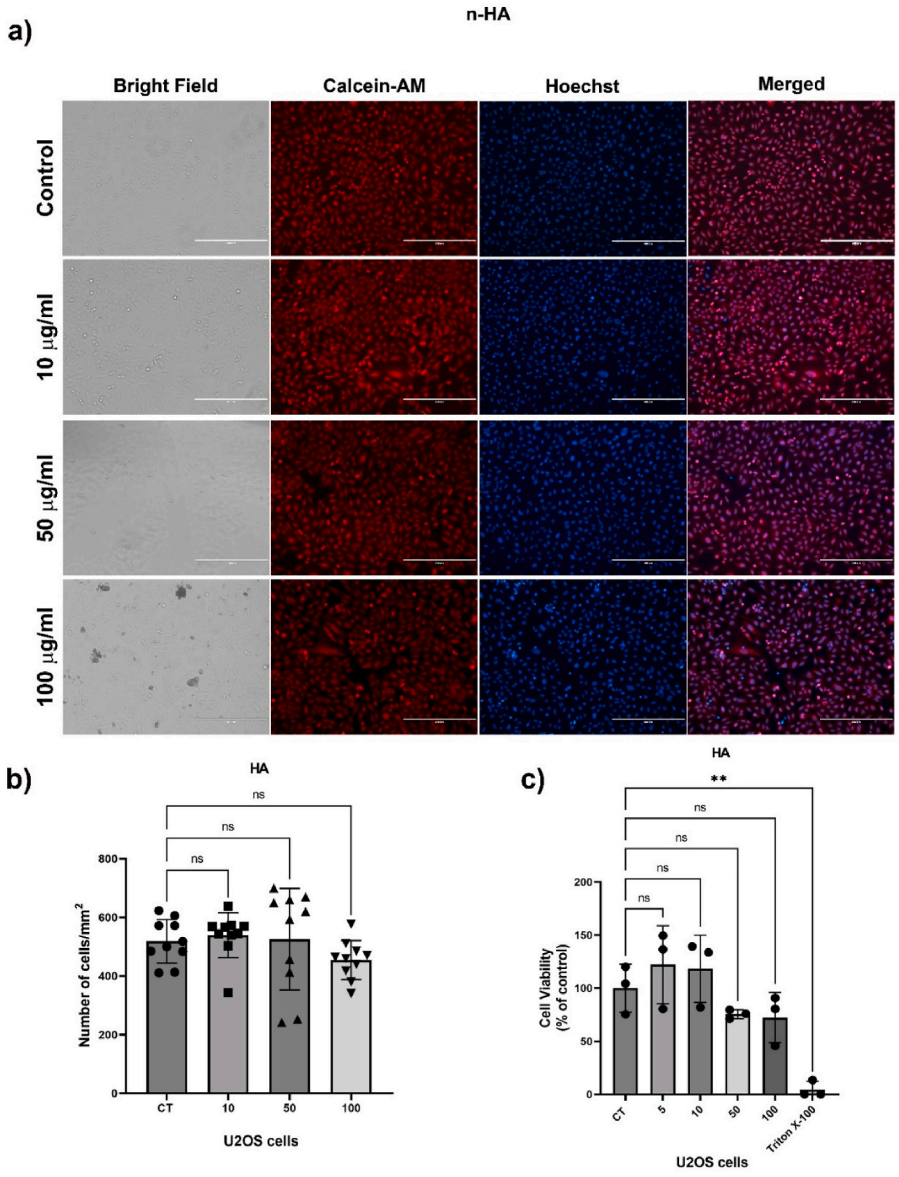

Fig. 11. Cell proliferation and cell viability assays on U2OS cells treated with HA. The cells were treated with n-HA using the following concentrations 10, 50, and 100 μg ml^{-1}. a) Cells were incubated with Calcein red-orange AM (in red) and Hoechst (in blue) to evaluate the cell viability and the number of cells, respectively. Then, cells were counted for each group using nuclear staining. b) The graph shows the number of cells/mm^2 from 10 images per group. Scale = 400 μm. Next, an MTT assay was used to evaluate the cell viability. c) The graph shows the normalized MTT data as a percentage of the control group (CT) from the cells treated with 5, 10, 50, and 100 μg ml^{-1} of n-HA. Cells treated with Triton-X 100 were used as a positive control for cell viability. ns = non-significant. **p < 0,01. (For interpretation of the references to colour in this figure legend, the reader is referred to the Web version of this article.)

thermal stability with low mass loss was already expected, due to the intrinsic characteristics of the material. Mass loss occurs in a single step at a slow rate. In the range of 25–150 °C, the mass loss can be attributed to the loss of interstitial water in the hydroxyapatite crystals. However, the sample continues to show a small loss of mass up to 500 °C, when the loss of mass stabilizes. This mass loss may probably be related to the removal of some possible residue from the surfactant used in the synthesis of n-HA.

The degradation of CMAP-HA occurs in two steps at slow rates. The first starts at room temperature and goes up to approximately 226 °C, presenting a mass loss of 1.99%, The second presents a mass loss of 7.5% starting at 226 °C–726 °C. Comparing the thermal profile of CMAP with that of CMAP-HA, it is possible to perceive a similarity between the degradation steps. Both samples start the second step of degradation at a temperature of around 220 °C. However, the percentages of mass loss of CMAP-HA are much lower compared to CMAP. This is due to the presence of n-HA, which has high thermal stability.

Considering the small percentage of mass lost by n-HA, about 7.5% of the mass of CMAP was incorporated into the hydroxyapatite nanorods. However, it is not possible to determine the individual percentage of CM and APTES, but the interactions between these moieties and the materials' surface were systematically evaluated using X-ray photoelectron spectroscopy, as discussed in the section below.

The thermal analysis was also used to infer the degree of functionalization of CM and APTES anchored in the HA materials. The curves obtained through the DSC analysis of curcumin, APTES, and CMAP are shown in Fig. 8b. The curcumin DSC curve showed a sharp endothermic peak at 177.4 °C which corresponds to the melting point of curcumin. APTES shows an intense endothermic peak at 137.3 °C, and two smaller peaks at 147.7 °C and 155.2 °C. The CMAP sample showed a peak at 177.5 °C which corresponds to the melting temperature of the curcumin crystals. The existence of this peak indicates the presence of free curcumin that did not react with APTES, being present only as a physical mixture. The peak at 167.4 °C does not correspond to any APTES or curcumin peak, which indicates the formation of a new compound. Changes in exothermic and endothermic peaks are usually associated with interactions between compounds [93,94]. Therefore, this is further evidence that the modification of curcumin with APTES allowed the anchoring of curcumin to hydroxyapatite nanorods.

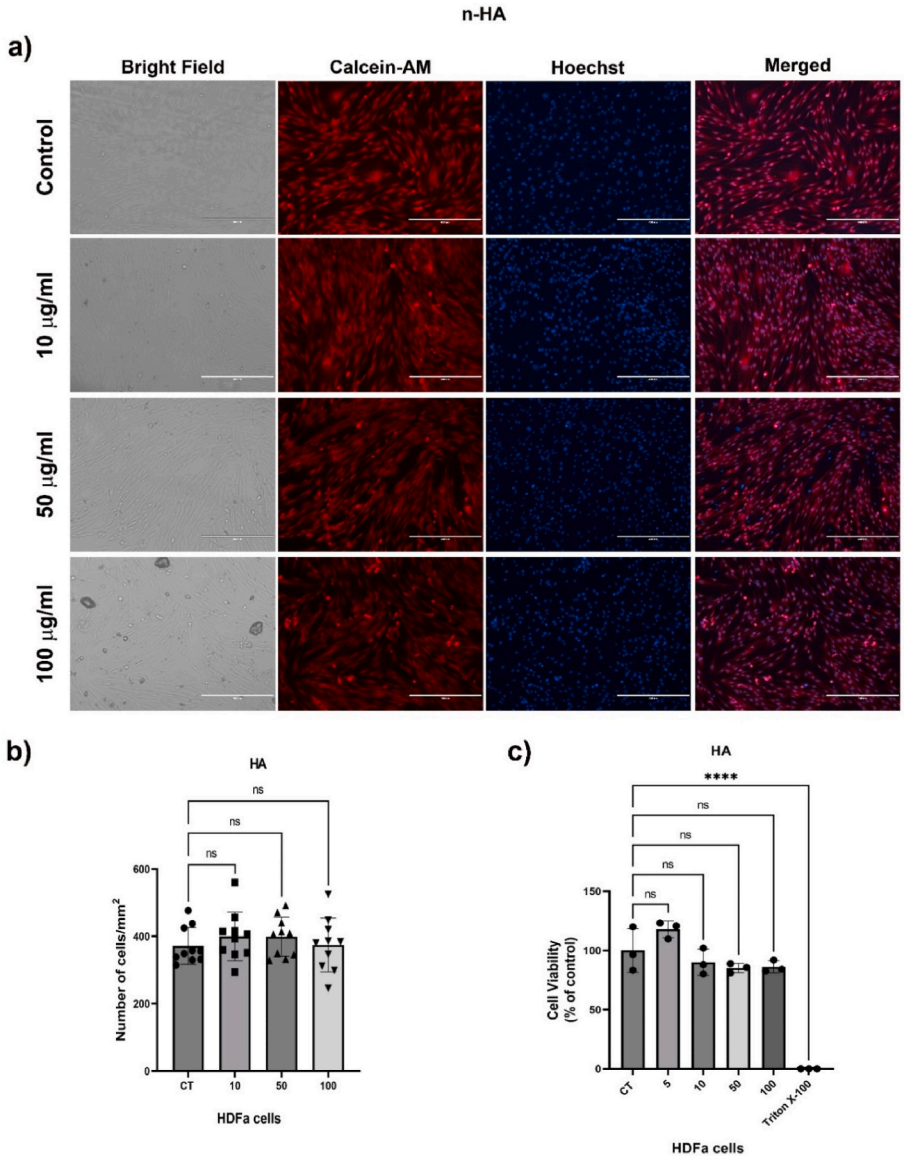

Fig. 12. Cell proliferation and cell viability assays on HDFa cells treated with n-HA. The cells were treated with n-HA using the following concentrations 10, 50, and 100 μg ml^{-1}. a) Cells were incubated with Calcein red-orange AM (in red) and Hoechst (in blue) to evaluate the cell viability and the number of cells, respectively. Then, cells were counted for each group using nuclear staining. b) The graph shows the number of cells/mm^2 from 10 images per group. Scale = 400 μm. Next, an MTT assay was used to evaluate the cell viability. c) The graph shows the normalized MTT data as a percentage of the control group (CT) from the cells treated with 5, 10, 50, and 100 μg ml^{-1} of n-HA. Cells treated with Triton-X 100 were used as a positive control for cell viability. ns = non-significant. ****$p < 0{,}0001$. (For interpretation of the references to colour in this figure legend, the reader is referred to the Web version of this article.)

3.8. Hydroxyapatite-CMAP interaction stability assay

Thermogravimetric analysis was performed to investigate the stability of the interaction between aminated curcumin and hydroxyapatite nanorods. The test was evaluated by incubating the samples in simulated body fluid (SBF) at pH 7.4, under agitation, and at a temperature of 37 °C for different times of 2, 24, and 48 h. After each incubation time, the suspensions were filtered and dried in an oven for 24 h at 60 °C and the powders were investigated by TGA. The results are shown in Fig. 9.

As expected, after the incorporation of CMAP, there was an increase in mass loss of 23% before incubation, referring to the organic phase incorporated in the nanorods. After the incubation process, it was observed that the mass losses were lower than the reference sample (CMAP-HA -23%). As these samples were not previously washed, these small differences may be due to the excess of CMAP weakly adsorbed on the nanorods. In addition, it was not possible to observe a significant difference between the mass losses of the samples incubated in different periods of time. After 48 h of incubation, only 4.04% of CMAP was released during the stability test, and 18.98% of CMAP remained bounded in the hydroxyapatite nanorods, indicating that the functionalization process resulted in a material with stable interactions between the components.

The average mass loss of samples incubated in SBF was 19.57%. This result shows that there is no significant detachment of CMAP from the hydroxyapatite nanorods, as no significant variations in mass losses were observed as a function of incubation time. This indicates a strong interaction of CMAP with hydroxyapatite nanorods. Furthermore, as the sample was not washed with ethanol, this may be an indication that, even with excess CMAP, the nanostructure has the potential to prevent the release of curcumin.

3.9. X-ray photoelectron spectroscopy – XPS

The chemical analysis of the surface of the different samples was carried out by XPS. The XPS survey spectra of the CM, CMAP, and CMAP-HA samples are shown in Fig. 10a. For sample CM, only elements present in the chemical structure of CM are detected. In the CMAP spectrum, in addition to carbon and oxygen peaks, it may be observed peaks at the energies of 102.6 eV, corresponding to the Si 2s, which is attributed to silane groups of APTES, and at 399.6 eV, corresponding to N 1s, indicating a successful functionalization step. The survey spectrum of CMAP-HA showed more additional peaks, corresponding to P, and Ca, derived from the phosphate group of hydroxyapatites, suggesting that the hydroxyapatite is integrated into the structure of the sample. The

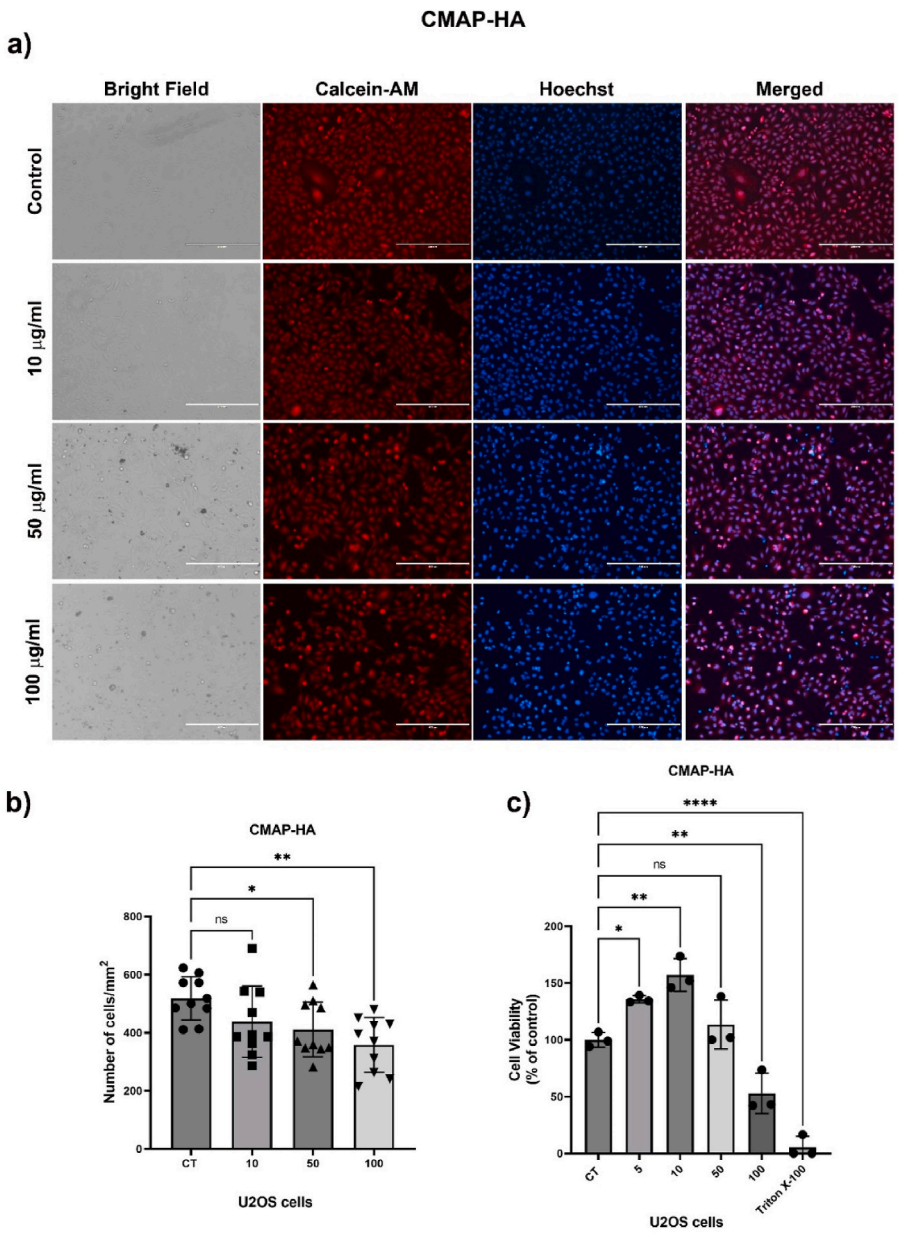

Fig. 13. Cell proliferation and cell viability assays on U2OS cells treated with CMAP-HA. The cells were treated with CMAP-HA using the following concentrations 10, 50, and 100 μg ml^{-1}. a) Cells were incubated with Calcein red-orange AM (in red) and Hoechst (in blue) to evaluate the cell viability and the number of cells, respectively. Then, cells were counted for each group using nuclear staining. b) The graph shows the number of cells/mm^2 from 10 images per group. Scale = 400 μm. Next, an MTT assay was used to evaluate the cell viability. c) The graph shows the normalized MTT data as a percentage of the control group (CT) from the cells treated with 5, 10, 50, and 100 μg ml^{-1} of CMAP-HA. Cells treated with Triton-X 100 were used as a positive control for cell viability. ns = non-significant. *p < 0,05, **p < 0,01, ****p < 0,0001. (For interpretation of the references to colour in this figure legend, the reader is referred to the Web version of this article.)

small F peak (1s) identified at 687.4 eV is probably resulted of some contamination of the hydroxyapatite, due to its ease of undergoing cationic and anionic substitutions. The chemical compositions, as obtained by XPS, and shown in Table 6, reflect the surface chemical modifications in the successive functionalization steps.

To investigate in more details the functionalization process, for the 3 samples high-resolution XPS spectra of C 1s, N 1s, and O 1s peaks were acquired. These peaks were adjusted with a sum of components that are associated with different species (different chemical bonds) present on the surface of the samples, as shown in Fig. 10(b–d), and discussed below. Fig. 10b shows the high-resolution XPS spectra of O s1 for the CM, CMAP, and CMAP-HA samples. For CM, it is possible to observe three components in the O 1s, with binding energies of 531.2 eV, 533.3 eV, and 536.3 eV, corresponding to C═O, C–OH and OH species of the phenol group, respectively. The O 1s spectrum of the CMAP sample, on the other hand, shows a principal component at 533.3 eV [95], attributed to Si–OH, which indicates that the Si–O bonds of APTES are dominant. During hydrolysis, the Si–O of APTES is converted into –OH groups, creating a good coupling agent between curcumin and hydroxyapatite molecules [96]. This suggests that the surface of the sample is likely covered by APTES molecules.

The deconvolution of the O 1s peak (Fig. 10 b) is questionable for the CMAP-HA sample since it is difficult to distinguish between O–C bonds and hydroxyapatite nanorod components, due to the strong superposition of binding energy values in this region. Assuming, as expected, that HA binds to the amine in CMAP-HA, the O 1s spectrum can be equipped with components belonging only to n-HA. Thus, it is possible to observe components with binding energies in 533.7 eV of P–O, in 533.0 eV, and in 532.0 eV of O–P–O bonds, referring to species of the phosphate group, and also a component at 529.9 eV, associated with O–Ca bonds [40]. This proposition indicates that HA is covering the surface of the sample.

The N 1s high-resolution spectrum of the CMAP sample is shown in Fig. 10c. The dominant peak is an amine, at 399.4 eV, and some protonated amine (at 400.8 eV) is present, indicating that in the functionalization of CMAPTES interacts with the oxygens of the CM chain, leaving the amine group free [96]. Another fact that supports this idea is the big reduction N 1s peak observed in the broad XPS spectrum of the

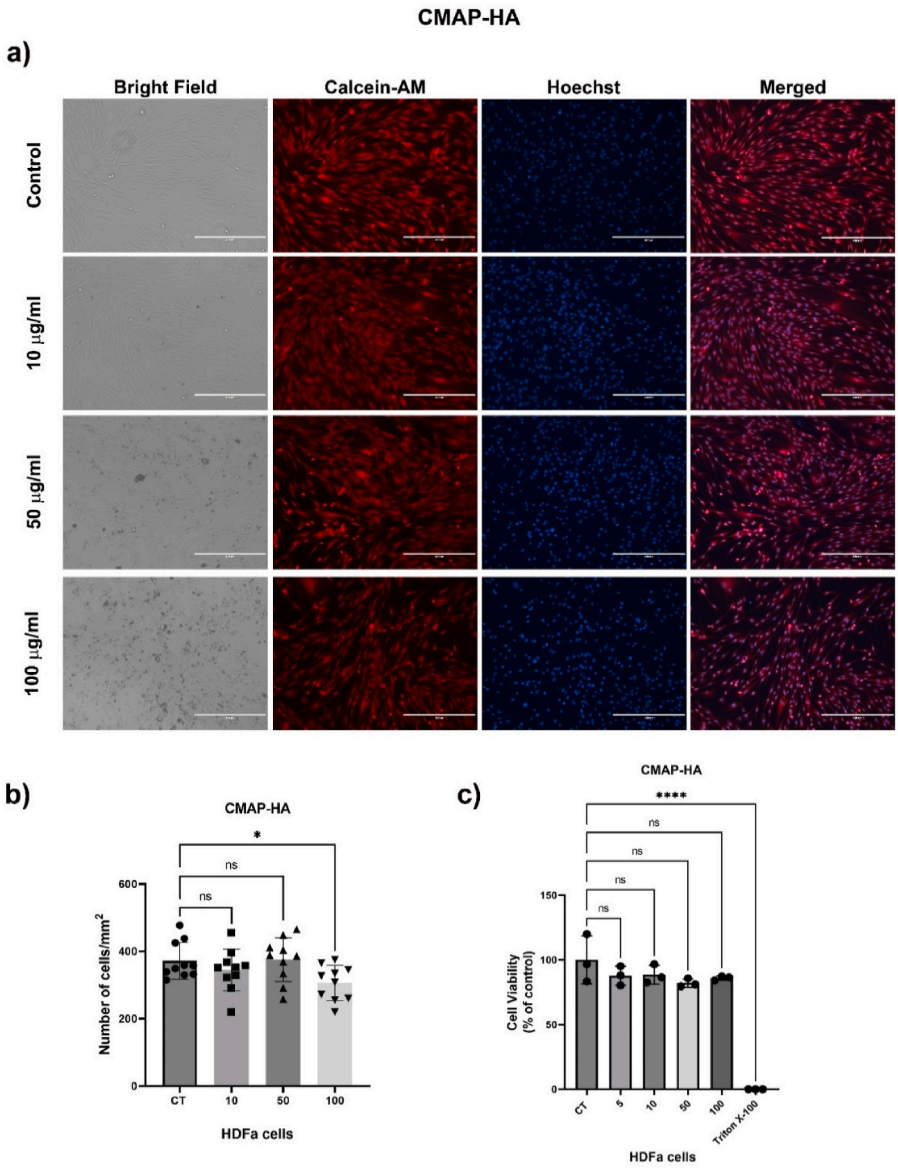

Fig. 14. Cell proliferation and cell viability assays on HDFa cells treated with CMAP-HA. The cells were treated with CMAP-HA using the following concentrations 10, 50, and 100 μg ml^{-1}. a) Cells were incubated with Calcein red-orange AM (in red) and Hoechst (in blue) to evaluate the cell viability and the number of cells, respectively. Then, cells were counted for each group using nuclear staining. b) The graph shows the number of cells/mm^2 from 10 images per group. Scale = 400 μm. Next, an MTT assay was used to evaluate the cell viability. c) The graph shows the normalized MTT data as a percentage of the control group (CT) from the cells treated with 5, 10, 50, and 100 μg ml^{-1} of CMAP-HA. Cells treated with Triton-X 100 were used as a positive control for cell viability. ns = non-significant. *p < 0,05, ****p < 0,0001. (For interpretation of the references to colour in this figure legend, the reader is referred to the Web version of this article.)

CMAP- HA sample (see Fig. 10c), which may indicate that the amine bounds to HA. Unfortunately, the N 1s signal is so small for the CMAP-HA sample that a reasonable fit of this peak was not possible.

Another possibility that may justify this result is that the amount of CMAP bound to n-HA may be very small, as discussed in the TG and XRD results. As in the filtering process after the functionalization, the CMAP-HA sample was washed with excess ethanol, and all the CMAP that was not bound was removed, significantly reducing the intensity of the nitrogen peak in the sample. This result corroborates the DSC analysis, indicating that only a part of the CM was functionalized.

In the C 1s spectrum for sample CM (Fig. 10d), the component at 284.6 eV corresponds to the C–C and C═C sp2 bonds, and the components at 285.3, 286.4, and 287.2 eV are related to the C–C sp3, C–O, and C= O species, respectively [95]. For the CMAP sample, it is possible to observe the emergence of two new components in the C 1sE, changing the peak profile. The component at 285.7 eV is attributed to the C–N bonds of the amine group present in APTES, and the second one at 288.3 eV can be attributed to COOH species originated from some residual acetic acid used in the functionalization process. In the C 1s spectrum of the CMAP-HA sample (Fig. 10d), it is possible to observe the appearance of a new component, at 289.9 eV, that can be attributed to the carbonate ion present in the HA, as previously suggested from the analysis of the FTIR results, which may have been originated by the decomposition of CTAB, and the reaction of C with O2 during the calcination process [40]. If compared to the CMAP spectrum, it is also noticeable a reduction in the intensity of the C–C sp3 and C–C, C═C sp2 components, and an increase in the intensity of the C–N and C═O components. This increase may be related to some interaction of CMAP with HA.

The chemical analyses performed in this work combining XPS, FTIR, and DSC results and the stability assay, are in good agreement with the DFT predictions, showing that curcumin molecule can be chemically modified by APTES moiety to increase solubility and strongly bind to hydroxyapatite nanoparticles, aiming at a stable nanosystem designed for cancer treatments.

3.10. Cell proliferation and cell viability assays

Curcumin has been demonstrated to have anti-neoplastic properties and cell proliferation inhibition in tumoural cells [23,24]. It is described that the viability of human osteosarcoma cells U2OS was reduced upon curcumin treatment [97]. Cell counting and MTT assays were performed to evaluate the potential of CMAP-HA as a new candidate for

osteosarcoma therapy. The n-HA and CMAP-HA nanomaterials were tested using the following concentrations 5, 10, 50, and 100 μg ml^{-1}. The n-HA treatment did not affect U2OS and HDFa proliferation (Fig. 11 a-b and 12 a-b) and cell viability (Figs. 11c and 12 c). However, the U20S cells treated with 100 μg ml^{-1} of CMAP-HA showed a reduction in the number of cells treated with 50 and 100 μg ml^{-1} respectively, $p < 0,05$ (Fig. 13a–b) and decreased cell viability, $p < 0,01$ (Fig. 13c). The primary fibroblasts showed no difference between CMAP-HA treated groups and showed a decrease in the number of cells only with 100 μg ml^{-1} (Fig. 14 a-b), $p < 0,05$. As a positive control, it was used 0,5% Triton X-100. These results demonstrated that CMAP-HA has a potential anti-neoplastic effect on osteosarcoma cells. Curcumin is also reported to have a dual impact by suppressing osteosarcoma development while repairing bone abnormalities [97]. Taken altogether, the combination of CM with HA could be an exceptional option for osteosarcoma therapy.

4. Conclusion

Based on the results obtained, it is possible to state that hydroxyapatite nanorods were successfully synthesized. The FTIR results indicated the obtaining of carbonated hydroxyapatite. The presence of any other crystalline phase in the sample was not observed, which indicates the obtaining of suitable nanohydroxyapatite for the desired application. The images obtained by the transmission microscope confirmed the rod-shaped morphology of nanohydroxyapatite. The synthesized nanorods presented pores throughout their structure, due to the surfactant leaving in the calcination step. The thermal stability of n-HA was confirmed by TG and DSC characterization techniques. Considering all the limitations of curcumin, such as low solubility, low stability, and photodegradation among other difficulties, the functionalization of curcumin with APTES proved to be a simple and viable method. The overall DFT predictions show that curcumin molecules can be chemically modified by APTES moiety considering ΔG values as the energetically favorable to occur among the proposed ones. The results showed no evidence that curcumin was degraded during the process. Changes in its structure allowed its incorporation into hydroxyapatite nanorods. Cell viability and the number of osteosarcoma cells were decreased by CMAP-HA treatment. The combination of CM with HA could be a promising candidate for osteosarcoma treatment. In general, the synthesized nanostructure presented suitable characteristics for carrying out further biological assays in vitro and later for initial assays in vivo, thus allowing for evaluating its potential for osteosarcoma therapy.

Declaration of competing interest

The authors declare that they have no known competing financial interests or personal relationships that could have appeared to influence the work reported in this paper.

Acknowledgments

This research was supported by the Fundação de Amparo á Pesquisa do Estado de Minas Gerais - FAPEMIG, Conselho Nacional de Desenvolvimento Científico e Tecnológico - CNPq and Coordenação de Aperfeiçoamento de Pessoal de Nível Superior - CAPES. The authors thank the Microscopy Center of the Federal University of Minas Gerais, Belo Horizonte, Brazil for the analyses involving electron microscopy. M.J.S.M. and R.J.C.B acknowledge financial support from the Brazilian Institute of Science and Technology (INCT) in Carbon Nanomaterials, Rede Mineira de Materiais Bidimensionais (FAPEMIG), and Financiadora de Estudos e Projetos (FINEP). We would like to thank the Center for Information Technology of the University of Groningen for their support and for providing access to the Peregrine high-performance computing cluster.

Appendix A. Supplementary data

Supplementary data to this article can be found online at https://doi.org/10.1016/j.ceramint.2023.03.115.

References

[1] Ministério da Saúde, Tipos de câncer | INCA - Instituto Nacional de Câncer, Osteossarcoma, 2022. https://www.inca.gov.br/tipos-de-cancer/cancer-infanto juvenil/osteossarcoma/profissional-de-saude. (Accessed 7 July 2022).
[2] PDQ Pediatric Treatment Editorial Board, Osteosarcoma and Malignant Fibrous Histiocytoma of Bone Treatment (PDQ®): Health Professional Version, PDQ Cancer Inf. Summ., 2002. http://www.ncbi.nlm.nih.gov/pubmed/26389179. (Accessed 8 July 2022).
[3] Key Statistics for Osteosarcoma, n.d. https://www.cancer.org/cancer/osteosarcoma/about/key-statistics.html. (Accessed 7 July 2022).
[4] S.A. Savage, L. Mirabello, Using epidemiology and genomics to understand osteosarcoma etiology, Sarcoma 2011 (2011) 1–13, https://doi.org/10.1155/2011/548151.
[5] B. Tan, Y. Wu, Y. Wu, K. Shi, R. Han, Y. Li, Z. Qian, J. Liao, Curcumin-Microsphere/IR820 hybrid bifunctional hydrogels for in situ osteosarcoma chemo- co-thermal therapy and bone reconstruction, ACS Appl. Mater. Interfaces 13 (2021) 31542–31553, https://doi.org/10.1021/acsami.1c08775.
[6] A.M. Czarnecka, K. Synoradzki, W. Firlej, E. Bartnik, P. Sobczuk, M. Fiedorowicz, P. Grieb, P. Rutkowski, Molecular biology of osteosarcoma, Cancers 12 (2020) 1–27, https://doi.org/10.3390/cancers12082130.
[7] L. Mirabello, R.J. Troisi, S.A. Savage, International osteosarcoma incidence patterns in children and adolescents, middle ages and elderly persons, Int. J. Cancer 125 (2009) 229–234, https://doi.org/10.1002/ijc.24320.
[8] R.L. Siegel, K.D. Miller, H.E. Fuchs, A. Jemal, Cancer statistics, 2021, CA, Cancer J. Clin. 71 (2021) 7–33, https://doi.org/10.3322/caac.21654.
[9] A. Misaghi, A. Goldin, M. Awad, A.A. Kulidjian, Osteosarcoma: a comprehensive review, Sicot-J. 4 (2018), https://doi.org/10.1051/sicotj/2017028.
[10] L. Ambrosio, M.G. Raucci, G. Vadalà, L. Ambrosio, R. Papalia, V. Denaro, Innovative biomaterials for the treatment of bone cancer, Int. J. Mol. Sci. 22 (2021) 1–19, https://doi.org/10.3390/ijms22158214.
[11] I. Corre, F. Verrecchia, V. Crenn, F. Redini, V. Trichet, The osteosarcoma microenvironment: a complex but targetable ecosystem, Cells 9 (2020) 1–25, https://doi.org/10.3390/cells9040976.
[12] C. Du, M. Zhou, F. Jia, L. Ruan, H. Lu, J. Zhang, B. Zhu, X. Liu, J. Chen, Z. Chai, Y. Hu, D-arginine-loaded metal-organic frameworks nanoparticles sensitize osteosarcoma to radiotherapy, Biomaterials 269 (2021), https://doi.org/10.1016/j.biomaterials.2020.120642.
[13] B. Wan, H. Hu, R. Wang, W. Liu, D. Chen, Therapeutic potential of circular RNAs in osteosarcoma, Front. Oncol. 10 (2020) 1–7, https://doi.org/10.3389/fonc.2020.00370.
[14] F. Verrecchia, F. Rédini, Transforming growth factor-β signaling plays a pivotal role in the interplay between osteosarcoma cells and their microenvironment, Front. Oncol. 8 (2018) 1–11, https://doi.org/10.3389/fonc.2018.00133.
[15] N. Soghli, G.A. Ferns, F. Sadeghsoltani, D. Qujeq, T. Yousefi, M. Vaghari-Tabari, MicroRNAs and osteosarcoma: potential targets for inhibiting metastasis and increasing chemosensitivity, Biochem. Pharmacol. 201 (2022), 115094, https://doi.org/10.1016/j.bcp.2022.115094.
[16] M. Tobeiha, A. Rajabi, A. Raisi, M. Mohajeri, S.M. Yazdi, A. Davoodvandi, F. Aslanbeigi, M.S. Vaziri, M.R. Hamblin, H. Mirzaei, Potential of natural products in osteosarcoma treatment: focus on molecular mechanisms, Biomed. Pharmacother. 144 (2021), 112257, https://doi.org/10.1016/j.biopha.2021.112257.
[17] L.D. Dias, K.C. Blanco, I.S. Mfouo-Tynga, N.M. Inada, V.S. Bagnato, Curcumin as a photosensitizer: from molecular structure to recent advances in antimicrobial photodynamic therapy, J. Photochem. Photobiol. C Photochem. Rev. 45 (2020), 100384, https://doi.org/10.1016/j.jphotochemrev.2020.100384.
[18] K.I. Priyadarsini, The chemistry of curcumin: from extraction to therapeutic agent, Molecules 19 (2014) 20091–20112, https://doi.org/10.3390/molecules191220091.
[19] V. Zoi, V. Galani, G.D. Lianos, S. Voulgaris, A.P. Kyritsis, G.A. Alexiou, The role of curcumin in cancer treatment, Biomedicines 9 (2021) 1–19, https://doi.org/10.3390/biomedicines9091086.
[20] M.D. Cas, R. Ghidoni, Dietary curcumin: correlation between bioavailability and health potential, Nutrients 11 (2019) 1–14, https://doi.org/10.3390/nu11092147.
[21] F.C. Rodrigues, N.V. Anil Kumar, G. Thakur, Developments in the anticancer activity of structurally modified curcumin: an up-to-date review, Eur. J. Med. Chem. 177 (2019) 76–104, https://doi.org/10.1016/j.ejmech.2019.04.058.
[22] S. Gunasekaran, R.K. Natarajan, S. Natarajan, R. Rathikha, Structural investigation on curcumin, Asian J. Chem. 20 (2008) 2903–2913.
[23] D.K. Walters, R. Muff, B. Langsam, W. Born, B. Fuchs, Cytotoxic effects of curcumin on osteosarcoma cell lines, Invest. N. Drugs 26 (2008) 289–297, https://doi.org/10.1007/s10637-007-9099-7.
[24] G. Wang, W. Song, N. Shen, H. Yu, M. Deng, Z. Tang, X. Fu, X. Chen, Curcumin-encapsulated polymeric nanoparticles for metastatic osteosarcoma cells treatment, Sci. China Mater. 60 (2017) 995–1007, https://doi.org/10.1007/s40843-017-9107-x.
[25] J.K. Patra, G. Das, L.F. Fraceto, E.V.R. Campos, M.D.P. Rodriguez-Torres, L. S. Acosta-Torres, L.A. Diaz-Torres, R. Grillo, M.K. Swamy, S. Sharma,

S. Habtemariam, H.S. Shin, Nano based drug delivery systems: recent developments and future prospects, J. Nanobiotechnol. 16 (2018) 1–33, https://doi.org/10.1186/s12951-018-0392-8.
[26] Y. Liu, Y. Tang, J. Wu, J. Sun, X. Liao, Z. Teng, G. Lu, Facile synthesis of biodegradable flower-like hydroxyapatite for drug and gene delivery, J. Colloid Interface Sci. 570 (2020) 402–410, https://doi.org/10.1016/j.jcis.2020.03.010.
[27] O.K. Koksal, G. Apaydin, E. Cengiz, L. Samek, H. Karahan, A. Tozar, M. Lankosz, Chemical analysis of hydroxyapatite artificial bone powders by energy dispersive X-ray fluorescence spectrometry (EDXRF), guang Pu xue yu guang Pu fen xi/spectroscopy spectr, Anal 38 (2018) 2645–2649, https://doi.org/10.3964/j.issn.1000-0593(2018)08-2645-05.
[28] A. Jin, Y. Wang, K. Lin, L. Jiang, Nanoparticles modified by polydopamine: working as "drug" carriers, Bioact. Mater. 5 (2020) 522–541, https://doi.org/10.1016/j.bioactmat.2020.04.003.
[29] M. Quadros, M. Momin, G. Verma, Design strategies and evolving role of biomaterial assisted treatment of osteosarcoma, Mater. Sci. Eng., C 121 (2021), 111875, https://doi.org/10.1016/j.msec.2021.111875.
[30] Y. Liu, D.B. Raina, S. Sebastian, H. Nagesh, H. Isaksson, J. Engellau, L. Lidgren, M. Tägil, Sustained and controlled delivery of doxorubicin from an in-situ setting biphasic hydroxyapatite carrier for local treatment of a highly proliferative human osteosarcoma, Acta Biomater. 131 (2021) 555–571, https://doi.org/10.1016/j.actbio.2021.07.016.
[31] V. Saxena, I. Shukla, L.M. Pandey, Elsevier Inc., 2019, https://doi.org/10.1016/B978-0-12-816909-4.00008-7 (Chapter 8). Hydroxyapatite: an inorganic ceramic for biomedical applications.
[32] S. Mondal, U. Pal, 3D hydroxyapatite scaffold for bone regeneration and local drug delivery applications, J. Drug Deliv. Sci. Technol. 53 (2019), 101131, https://doi.org/10.1016/j.jddst.2019.101131.
[33] Y. Hu, S. Cao, J. Chen, Y. Zhao, F. He, Q. Li, L. Zou, C. Shi, Biomimetic fabrication of icariin loaded nano hydroxyapatite reinforced bioactive porous scaffolds for bone regeneration, Chem. Eng. J. 394 (2020), 124895, https://doi.org/10.1016/j.cej.2020.124895.
[34] S. Bose, S. Tarafder, A. Bandyopadhyay, Hydroxyapatite Coatings for Metallic Implants, Elsevier Ltd., 2015, https://doi.org/10.1016/b978-1-78242-033-0.00007-9.
[35] N. Kumar, S. Ali, B. Kumar, M.S. Zafar, Z. Khurshid, Hydroxyapatite and Nanocomposite Implant Coatings, Elsevier Ltd, 2020, https://doi.org/10.1016/b978-0-12-819586-4.00005-6.
[36] R. Chen, J. Shi, B. Zhu, L. Zhang, S. Cao, Mesoporous hollow hydroxyapatite capped with smart polymer for multi-stimuli remotely controlled drug delivery, Microporous Mesoporous Mater. 306 (2020), 110447, https://doi.org/10.1016/j.micromeso.2020.110447.
[37] W. Li, F. Han, H. Liu, X. Niu, L. Shi, The synthesis of sulfate doped hydroxyapatite for enhanced drug loading and chemotherapeutic drug delivery towards lung cancer treatment, Ceram. Int. 46 (2020) 28578–28584, https://doi.org/10.1016/j.ceramint.2020.08.015.
[38] Z. Liu, J.D. Smart, A.S. Pannala, Recent developments in formulation design for improving oral bioavailability of curcumin: a review, J. Drug Deliv. Sci. Technol. 60 (2020), 102082, https://doi.org/10.1016/j.jddst.2020.102082.
[39] M.F. Cipreste, W. da N. Mussel, J. Batista da Silva, M.B. de Freitas Marques, R.J. C. Batista, P.L. Gastelois, W.A. de A. Macedo, E.M.B. de Sousa, A new theranostic system for bone disorders: functionalized folate-MDP hydroxyapatite nanoparticles with radiolabeled copper-64, Mater. Chem. Phys. 254 (2020), 123265, https://doi.org/10.1016/j.matchemphys.2020.123265.
[40] M.F. Cipreste, A.M. Peres, A.A.C. Cotta, F.H. Aragón, A. de M. Antunes, A.S. Leal, W.A.A. Macedo, E.M.B. de Sousa, Synthesis and characterization of 159 Gd-doped hydroxyapatite nanorods for bioapplications as theranostic systems, Mater. Chem. Phys. 181 (2016) 301–311, https://doi.org/10.1016/j.matchemphys.2016.06.063.
[41] S. Zhang, X. Ma, D. Sha, J. Qian, Y. Yuan, C. Liu, A novel strategy for tumor therapy: targeted, PAA-functionalized nano-hydroxyapatite nanomedicine, J. Mater. Chem. B. 8 (2020) 9589–9600, https://doi.org/10.1039/d0tb01603a.
[42] A. Izadi, A. Meshkini, M.H. Entezari, Mesoporous superparamagnetic hydroxyapatite nanocomposite: a multifunctional platform for synergistic targeted chemo-magnetotherapy, Mater. Sci. Eng., C 101 (2019) 27–41, https://doi.org/10.1016/j.msec.2019.03.066.
[43] S. Ghosh, R.S.K. Raju, N. Ghosh, K. Chaudhury, S. Ghosh, I. Banerjee, N. Pramanik, Development and physicochemical characterization of doxorubicin-encapsulated hydroxyapatite–polyvinyl alcohol nanocomposite for repair of osteosarcoma-affected bone tissues, Compt. Rendus Chem. 22 (2019) 46–57, https://doi.org/10.1016/j.crci.2018.10.005.
[44] R. Wang, W. Liu, Q. Wang, G. Li, B. Wan, Y. Sun, X. Niu, D. Chen, W. Tian, Anti-osteosarcoma effect of hydroxyapatite nanoparticles both: in vitro and in vivo by downregulating the FAK/PI3K/Akt signaling pathway, Biomater. Sci. 8 (2020) 4426–4437, https://doi.org/10.1039/d0bm00898b.
[45] M.F. Cipreste, M.R. de Rezende, M.L. Hneda, A.M. Peres, A.A.C. Cotta, V. de C. Teixeira, W.A. de A. Macedo, E.M.B. de Sousa, Functionalized-radiolabeled hydroxyapatite/tenorite nanoparticles as theranostic agents for osteosarcoma, Ceram. Int. 44 (2018) 17800–17811, https://doi.org/10.1016/j.ceramint.2018.06.248.
[46] R.C.R. dos Apostolos, M.F. Cipreste, R.G. de Sousa, E.M.B. de Sousa, Multifunctional hybrid nanosystems based on mesoporous silica and hydroxyapatite nanoparticles applied as potential nanocarriers for theranostic applications, J. Nanoparticle Res. 22 (2020), https://doi.org/10.1007/s11051-020-05105-0.
[47] M. Di Francesco, F. Pastorino, M. Ferreira, A. Fragassi, V. Di Francesco, A. L. Palange, C. Celia, L. Di Marzio, M. Cilli, V. Bensa, M. Ponzoni, P. Decuzzi, Augmented efficacy of nano-formulated docetaxel plus curcumin in orthotopic models of neuroblastoma, Pharmacol. Res. 188 (2023), 106639, https://doi.org/10.1016/j.phrs.2022.106639.
[48] M. Ashrafizadeh, A. Zarrabi, F. Hashemi, E.R. Moghadam, F. Hashemi, M. Entezari, K. Hushmandi, R. Mohammadinejad, M. Najafi, Curcumin in cancer therapy: a novel adjunct for combination chemotherapy with paclitaxel and alleviation of its adverse effects, Life Sci. 256 (2020), https://doi.org/10.1016/j.lfs.2020.117984.
[49] P. Fonseka, L. Gangoda, M. Pathan, D.G. Angela, S. Mathivanan, Combinatorial treatment of curcumin or silibinin with doxorubicin sensitises high-risk neuroblastoma, J. Cancer Metastasis Treat. 2020 (2020), https://doi.org/10.20517/2394-4722.2019.024.
[50] O.A. Hamed, N. Mehdawi, A.A. Taha, E.M. Hamed, M.A. Al-Nuri, A.S. Hussein, Synthesis and antibacterial activity of novel curcumin derivatives containing heterocyclic moiety, Iran, J. Pharm. Res. 12 (2013) 47–56, https://doi.org/10.22037/ijpr.2013.1243.
[51] P. Hohenberg, W. Kohn, Inhomogeneous electron gas, Phys. Rev. 136 (1964) 864–871, https://doi.org/10.1007/BF01198136.
[52] W. Kohn, L. Sham, Self-consistent equations including exchange and correlation effects, Phys. Rev. 140 (1965) 1133–1138.
[53] E. Runge, E. Gross, Density-functional theory for time-dependent systems, Phys. Rev. Lett. 52 (1984) 997–1000, https://doi.org/10.1103/PhysRevA.34.529.
[54] Vrije Universiteit, CSM Theoretical Chemistry, 2022.
[55] P.J. Stephen, F.J. Devlin, C.F. Chabalowski, M.J. Frisch, Ab initio calculation of vibrational absorption, J. Phys. Chem. 98 (1994) 11623–11627.
[56] Y. Zhao, D.G. Truhlar, A new local density functional for main-group thermochemistry, transition metal bonding, thermochemical kinetics, and noncovalent interactions, J. Chem. Phys. 125 (2006), https://doi.org/10.1063/1.2370993.
[57] C.C. Pye, T. Ziegler, An implementation of the conductor-like screening model of solvation within the Amsterdam density functional package, Theor. Chem. Acc. 101 (1999) 396–408, https://doi.org/10.1007/s002140050457.
[58] A. Klamt, G. Schüürmann, COSMO: a new approach to dielectric screening in solvents with explicit expressions for the screening energy and its gradient, J. Chem. Soc. Perkin Trans. 2 (1993) 799–805, https://doi.org/10.1039/P29930000799.
[59] A. Klamt, Conductor-like screening model for real solvents: a new approach to the quantitative calculation of solvation phenomena, J. Phys. Chem. 99 (1995) 2224–2235, https://doi.org/10.1021/j100007a062.
[60] A. Klamt, V. Jonas, Treatment of the outlying charge in continuum solvation models, J. Chem. Phys. 105 (1996) 9972–9981, https://doi.org/10.1063/1.472829.
[61] N.L. Allinger, X. Zhou, J. Bergsma, Molecular mechanics parameters, J. Mol. Struct. THEOCHEM. 312 (1994) 69–83, https://doi.org/10.1016/S0166-1280(09)80008-0.
[62] Rapid colorimetric assay for cellular growth and survival: application to proliferation and cytotoxicity assays, J. Immunol. Methods (1983) 55–63, https://doi.org/10.1016/0022-1759.
[63] C.A. Schneider, W.S. Rasband, K.W. Eliceiri, NIH Image to ImageJ: 25 years of image analysis, Nat. Methods 9 (2012) 671–675, https://doi.org/10.1038/nmeth.2089.
[64] L. Pinto, Quantikov Image Analyser, 1996.
[65] H. Madupalli, B. Pavan, M.M.J. Tecklenburg, Carbonate substitution in the mineral component of bone: discriminating the structural changes, simultaneously imposed by carbonate in A and B sites of apatite, J. Solid State Chem. 255 (2017) 27–35, https://doi.org/10.1016/j.jssc.2017.07.025.
[66] D.S. Gomes, A.M.C. Santos, G.A. Neves, R.R. Menezes, A brief review on hydroxyapatite production and use in biomedicine, Ceramica 65 (2019) 282–302, https://doi.org/10.1590/0366-69132019653742706.
[67] N.A.S. Mohd Pu'ad, R.H. Abdul Haq, H. Mohd Noh, H.Z. Abdullah, M.I. Idris, T. C. Lee, Synthesis method of hydroxyapatite: a review, Mater, Today Proc. 29 (2019) 233–239, https://doi.org/10.1016/j.matpr.2020.05.536.
[68] R.K. Biswas, P. Khan, S. Mukherjee, A.K. Mukhopadhyay, J. Ghosh, K. Muraleedharan, Study of short range structure of amorphous Silica from PDF using Ag radiation in laboratory XRD system, Raman and NEXAFS, J. Non-Cryst. Solids 488 (2018) 1–9, https://doi.org/10.1016/j.jnoncrysol.2018.02.037.
[69] L.D. Pompeu, M.G. Finger, V.D.A. Severo, L. Pinheiro, Evaluation of stability of aqueous dispersions using zeta potential data, Discip. Sci. 19 (2018) 381–388.
[70] J. Moore, E. Cerasoli, Particle light scattering methods and applications, Encycl. Spectrosc. Spectrom. (2010) 2077–2088, https://doi.org/10.1016/B978-0-12-374413-5.00040-3.
[71] H.J. Kim, S.H. Kim, H.M. Kim, Y.S. Kim, J.M. Oh, Surface roughness effect on the cellular uptake of layered double hydroxide nanoparticles, Appl. Clay Sci. 202 (2021), 105992, https://doi.org/10.1016/j.clay.2021.105992.
[72] M. Ma, Y. Chen, M. Zhao, J. Sui, Z. Guo, Y. Yang, Z. Xu, Y. Sun, Y. Fan, X. Zhang, Hierarchical responsive micelle facilitates intratumoral penetration by acid-activated positive charge surface and size contraction, Biomaterials 271 (2021) 1–14, https://doi.org/10.1016/j.biomaterials.2021.120741.
[73] A. Verma, F. Stellacci, Effect of surface properties on nanoparticle-cell interactions, Small 6 (2010) 12–21, https://doi.org/10.1002/smll.200901158.
[74] V. Forest, J. Pourchez, Preferential binding of positive nanoparticles on cell membranes is due to electrostatic interactions: a too simplistic explanation that does not take into account the nanoparticle protein corona, Mater. Sci. Eng., C 70 (2017) 889–896, https://doi.org/10.1016/j.msec.2016.09.016.
[75] R. Augustine, A. Hasan, R. Primavera, R.J. Wilson, A.S. Thakor, B.D. Kevadiya, Cellular uptake and retention of nanoparticles: insights on particle properties and

interaction with cellular components, Mater. Today Commun. 25 (2020), 101692, https://doi.org/10.1016/j.mtcomm.2020.101692.
[76] A. Rajasekar, T. Devasena, S. Suresh, B. Senthil, R. Sivaramakrishnan, A. Pugazhendhi, Curcumin nanospheres and nanorods: synthesis, characterization and anticancer activity, Process Biochem. 112 (2021) 248–253, https://doi.org/10.1016/j.procbio.2021.12.007.
[77] A. Naqshbandi, A. Rahman, Synthesis and characterization of chlorinated hydroxyapatite as novel synthetic bone substitute with negative zeta potential, Ceram. Int. (2021), https://doi.org/10.1016/j.ceramint.2021.12.013.
[78] S. Jose, M. Senthilkumar, K. Elayaraja, M. Haris, A. George, A.D. Raj, S. J. Sundaram, A.K.H. Bashir, M. Maaza, K. Kaviyarasu, Preparation and characterization of Fe doped n-hydroxyapatite for biomedical application, Surface. Interfac. 25 (2021), 101185, https://doi.org/10.1016/j.surfin.2021.101185.
[79] S. Dhatchayani, S. Vijayakumar, N. Sarala, B. Vaseeharan, K. Sankaranarayanan, Effect of curcumin sorbed selenite substituted hydroxyapatite on osteosarcoma cells: an in vitro study, J. Drug Deliv. Sci. Technol. 60 (2020), 101963, https://doi.org/10.1016/j.jddst.2020.101963.
[80] V. Prakash, I. Venda, V. Thamizharasi, Synthesis and characterization of surfactant assisted hydroxyapatite powder using microemulsion method, Mater. Today Proc. (2021), https://doi.org/10.1016/j.matpr.2021.05.059.
[81] I.R. Gibson, Natural and synthetic hydroxyapatites, in: M.J.Y. Wagner, R. William, Guigen Zhang, Shelly E. Sakiyama-Elbert (Eds.), Biomater. Sci., fourth ed., Elsevier, 2020, pp. 307–317, https://doi.org/10.1016/B978-0-12-816137-1.00023-4.
[82] F. Chen, M. Wang, J. Wang, X. Chen, X. Li, Y. Xiao, X. Zhang, Effects of hydroxyapatite surface nano/micro-structure on osteoclast formation and activity, J. Mater. Chem. B. 7 (2019) 7574–7587, https://doi.org/10.1039/c9tb01204d.
[83] K. Eddahaoui, S. Benmokhtar, B. Manoun, S. Belaaouad, P. Lazor, Vibrational spectra and factor group analysis of M0.50TiOPO 4 oxyphosphates (M = Mg, Zn, Ni, Co, Fe and Cu), Spectrochim. Acta Part A Mol. Biomol. Spectrosc. 99 (2012) 81–89, https://doi.org/10.1016/j.saa.2012.08.033.
[84] W.H. Lee, R. Rohanizadeh, C.Y. Loo, In situ functionalizing calcium phosphate biomaterials with curcumin for the prevention of bacterial biofilm infections, Colloids Surf. B Biointerfaces 206 (2021), 111938, https://doi.org/10.1016/j.colsurfb.2021.111938.
[85] C. Suresh Kumar, K. Dhanaraj, R.M. Vimalathithan, P. Ilaiyaraja, G. Suresh, Hydroxyapatite for bone related applications derived from sea shell waste by simpleprecipitation method, J. Asian Ceram. Soc. 8 (2020) 416–429, https://doi.org/10.1080/21870764.2020.1749373.
[86] T.M. Kolev, E.A. Velcheva, B.A. Stamboliyska, M. Spiteller, DFT and experimental studies of the structure and vibrational spectra of curcumin, Int. J. Quant. Chem. 102 (2005) 1069–1079, https://doi.org/10.1002/qua.20469.
[87] R.N. Oliveira, M.C. Mancini, F.C.S. de Oliveira, T.M. Passos, B. Quilty, R.M. da, S. M. Thiré, G.B. McGuinness, Análise por FTIR e quantificação de fenóis e flavonóides de cinco produtos naturais disponíveis comercialmente utilizados no tratamento de feridas, Rev. Mater. 21 (2016) 767–779, https://doi.org/10.1590/S1517-707620160003.0072.
[88] C. Chignell, P. Bilski, K. Reszka, A. Motien, R. Sik, T. Dahl, Spectral and photochemical properties of curcumin, Photochem. Photobiol. 59 (1994) 295–302.
[89] X. Zarate, I. González P, S. Caramori, E. Benazzi, T. Barra, L. Arrue, Y. nan Wu, C. Díaz-Uribe, W. Vallejo, E. Schott, Experimental and DFT study of natural curcumin derived dyes as n-type sensitizers, Sol. Energy 225 (2021) 305–315, https://doi.org/10.1016/j.solener.2021.06.051.
[90] F.J.A. Ferrer, J. Cerezo, E. Stendardo, R. Improta, F. Santoro, Insights for an accurate comparison of computational data to experimental absorption and emission spectra: beyond the vertical transition approximation, J. Chem. Theor. Comput. 9 (2013) 2072–2082, https://doi.org/10.1021/ct301107m.
[91] D. Jacquemin, V. Wathelet, E.A. Perpète, C. Adamo, Extensive TD-DFT benchmark: singlet-excited states of organic molecules, J. Chem. Theor. Comput. 5 (2009) 2420–2435, https://doi.org/10.1021/ct900298e.
[92] Z. Chen, Y. Xia, S. Liao, Y. Huang, Y. Li, Y. He, Z. Tong, B. Li, Thermal degradation kinetics study of curcumin with nonlinear methods, Food Chem. 155 (2014) 81–86, https://doi.org/10.1016/j.foodchem.2014.01.034.
[93] R. Govindaraju, R. Karki, J. Chandrashekarappa, M. Santhanam, A.K.K. Shankar, H.K. Joshi, G. Divakar, Enhanced water dispersibility of curcumin encapsulated in alginate-polysorbate 80 nano particles and bioavailability in healthy human volunteers, Pharm. Nanotechnol. 7 (2019) 39–56, https://doi.org/10.2174/2211738507666190122121242.
[94] R.S. Nair, A. Morris, N. Billa, C.O. Leong, An evaluation of curcumin-encapsulated chitosan nanoparticles for transdermal delivery, AAPS PharmSciTech 20 (2019) 1–13, https://doi.org/10.1208/s12249-018-1279-6.
[95] P. Khandelwal, A. Alam, A. Choksi, S. Chattopadhyay, P. Poddar, Retention of anticancer activity of curcumin after conjugation with fluorescent gold quantum clusters: an in vitro and in vivo xenograft study, ACS Omega 3 (2018) 4776–4785, https://doi.org/10.1021/acsomega.8b00113.
[96] I. Berktas, A.N. Ghafar, P. Fontana, A. Caputcu, Y. Menceloglu, B.S. Okan, Facile synthesis of graphene from waste tire/silica hybrid additives and optimization study for the fabrication of thermally enhanced cement grouts, Molecules 25 (2020) 886, https://doi.org/10.3390/molecules25040886.
[97] F. Zahedipour, M. Bolourinezhad, Y. Teng, A. Sahebkar, The multifaceted therapeutic mechanisms of curcumin in osteosarcoma: state-of-the-art, JAMA Oncol. 2021 (2021), https://doi.org/10.1155/2021/3006853.